Mixed Species Ion Chains for Scalable Quantum Computation

John Albert Wright

A dissertation
submitted in partial fulfillment of the
requirements for the degree of

Doctor of Philosophy

University of Washington

2015

Reading Committee:

Boris Blinov, Chair

Subhadeep Gupta

Xiaodong Xu

Program Authorized to Offer Degree:
Department of Physics

University of Washington

Abstract

Mixed Species Ion Chains for Scalable Quantum Computation

John Albert Wright

Chair of the Supervisory Committee:
Associate Professor Boris Blinov
Department of Physics

Mixed species chains of barium and ytterbium ions are investigated as a tool for building scalable quantum computation devices. Ytterbium ions provide a stable environmentally-insensitive qubit that is easily initialized and manipulated, while barium ions are easily entangled with photons that can allow quantum information to be shared between systems in multiple quantum computation units. Barium and ytterbium are trapped in a linear chain in a Paul trap and their normal mode structure and thermal occupation numbers are measured with a narrow fiber laser addressing a quadrupole transition to evaluate the suitability of the scheme. Planar surface traps with many DC electrodes provide the ability to reorder the chain of ions to optimize normal mode cooling, and initial attempts to realize this capability are discussed. Transferring quantum information between ions in the chain requires lasers with large Lamb-Dicke parameters to provide good coupling to the motional degrees of freedom of the chain. For this reason, a mode-locked Raman system is developed and initial measurements of qubit rotations are shown.

TABLE OF CONTENTS

Page

LIST OF FIGURES

Figure Number Page

LIST OF TABLES

Table Number Page

ABBREVIATIONS

ADC Analog to Digital Converter. Converts analog voltage or current signals to the digital representation of a corresponding number in Volts of Amperes.

AOM Acousto-Optic Modulator. Device to diffract an incoming laser beam against a standing wave of RF. Allows the frequency and power of a diffracted beam to be quickly controlled by changing RF parameters.

DAC Digital to Analog Converter. Converts a digital representation of a number to a corresponding analog signal of that many Volts or Amperes.

ECDL External Cavity Diode Laser. Laser made by externally frequency selecting and feeding back light into a laser diode.

HWP Half Wave Plate. Delays light polarized along one direction by half a wavelength while not affecting the orthogonal direction of polarization.

PBS Polarizing Beam Splitter. Reflects light polarized along one direction while transmitting the orthogonal direction of polarization.

QWP Quarter Wave Plate. Delays light polarized along one direction by a quarter of a wavelength while not affecting the orthogonal direction of polarization.

UHV Ultra-high vacuum. Pressures below 10^{-9} torr. Usually only achievable with all metal seals and careful chamber preparation.

ACKNOWLEDGMENTS

I would like to thank my parents, Juli and William Wright, and my stepmother, Ellen Fox, for working hard to raise me well and provide me with all the opportunities I could hope for. I also have to thank my wonderful wife, Allison Wootan. We have been a huge part of each others' lives for almost a decade now, and I can't imagine being here without her. Without the love and support of these people I certainly would not have made it to where I am today.

I would also like to thank Boris Blinov for his support since the first day I arrived at the University of Washington. He's given me the opportunity to take apart everything in our lab, and I've even managed to put most of it back together. I can't imagine working in any other kind of lab, and I've greatly enjoyed it and learned so much from him.

I've been fortunate to work with a great team of graduate students and postdoctoral researchers. In particular, I learned a huge fraction of what I know about ion trapping by talking with fellow graduate students Thomas Noel and Matt Hoffman. It's been great working closely with Tomasz Sakrejda these past few years and seeing Carolyn Auchter, Spencer Williams, and CK Chou around the lab. I've also enjoyed working with our postdocs Richard Graham and Zichao Zhou. There have also been many undergraduates who have helped build so much of the infrastructure I use everyday including Matthew Bohman, Wen Lin Tan, Sarah Innes-Gold, Sean Nelson, and many others.

Part I

QUANTUM COMPUTATION IN ION TRAPS

Chapter 1

QUANTUM COMPUTATION

Quantum computation is a method for performing calculations on data that utitilizes additional properties of quantum mechanics that classical computation does not. Quantum algorithms running on capable systems will be able to perfom some calculations in exponentially less time than classical computers will ever be able to. To realize these speed increases, we need to engineer unprecedented control over hundreds or thousands of coupled quantum systems. There are a number of physical systems that have a sufficient degree of isolation from environmental noise that it is possible to consider implementing a quantum computer using them. These systems include superconducting junctions[**?**], quantum dots[**?**], trapped neutral atoms[**?**], and trapped ions.

1.1 Motivating Quantum Computing

In order to quantify the possible speed increase that quantum computers represent, it is useful to refer to the notion of complexity classes in computer science. Complexity classes are groups of problems that share a similar dependence between the input size of a problem and the time and memory required to solve it. In Figure **??**, PSPACE is the class of problems that can be solved using an amount of memory that is polynomial in the size of the problem. The size of the problem in this context refers to the size required to represent the inputs of the problem in computer memory. For example, if the input is a single number, N, it can be represented in space proportional to $\log N$. For problems that require the input of a large series of numbers, the logarithm of each number is approximately the same size and the problem size is often written as the number of input numbers ignoring the approximately constant multiplicative factor. The NP complexity class in the figure is the class of problems whose solutions can be verified in polynomial time, meaning an amount of computational time that depends via a polynomial on the size of the input. One

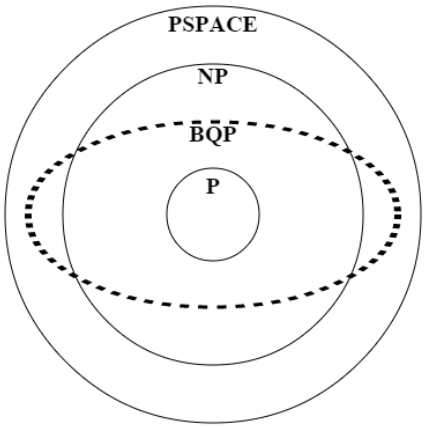

Figure 1.1: The currently believed relationship between the BQP complexity class and other classical computing complexity classes. BQP includes some problems from NP, but not all.

of the most important questions in computer science is whether these problems that can be verified in polynomial time can also be solved in polynomial time, and therefore are also a member of the complexity class P. It is generally believed that these complexity classes are not equal, that is $P \neq NP$, and therefore algorithms to efficiently solve NP problems of size will never be found. Instead we will have to use algorithms that scale poorly with the size of the problem, and can become difficult to solve even for problems that seem trivially small.

Quantum algorithms are analyzed as probabilistic algorithms that take into account the probability of the algorithm producing the wrong solution. The computational class of problems that are easily solved using a quantum computer is named bounded error quantum polynomial time, or BQP. It is the class of problems solvable in polynomial time on a quantum computer with a probability of failure that is less than $\frac{1}{3}$. We can see from Figure **??** that quantum computers will be able to efficiently solve some problems that will probably never be efficiently solved classically, including some problems in NP and some problems that are not.

The most famous and arguably useful quantum algorithm is known as Shor's algorithm.

It is an algorithm for solving the discrete logarithm problem. The inputs to the problem are two elements, a and b, of some finite group, G, and the desired output is an exponent, n, such that $a^n = b$. The trivial algorithm is to continuously exponentiate a to higher and higher powers, which takes time proportional to the number of elements of G. Since the input to the problem is two elements of G, the input size of the problem is proportional to $\log G$ and the naïve algorithm takes time exponential in this input size. Practically speaking, this problem has applications in cryptography for which groups with size 2^{256} or larger are often chosen, and therefore classical algorithms would require absurd amounts of computational time to find solutions. Solving this problem is the difficult task that keeps public key cryptographically secured information safe, and it is generally suspected that for sufficiently large groups it will never be solved on classical hardware.

Shor's algorithm provides a solution to the discrete logarithm problem that requires only time linear in the size of the input. A functional quantum computer of sufficient size could use this algorithm to break all known public key cryptography techniques using a very small amount of computational time. These encryption techniques fall into two groups, those based on factoring large integers and those based on solving for roots of elliptic curves in finite fields. Both of these problems are easy to solve in one direction, but very costly to solve in the opposite direction. Someone desiring to encrypt something can easily compute the result of these calculations for chosen parameters, but finding those parameters from the result is very difficult. Both of these known public-key cryptography problems are extremely susceptible to quantum computing.

From a physicist's point of view, perhaps the larger motivation for building a quantum computer is the ability to simulate difficult quantum systems. Trapped ion based quantum computers are beginning to approach being able to find results for physical problems that are very difficult for classical computers to solve. In particular, frustrated magnetic systems can already be simulated using trapped ions [**?**], but these systems are very difficult to solve classically even for only dozens of particles. Simulating full Hamiltonians of complicated systems may remain infeasible on classical computers for decades still, while because of their favorable scaling, quantum computers will be trivially able to do so.

1.2 The DiVincenzo Criteria

The operational units of a quantum computer are usually refered to as qubits (short for quantum bits). Qubits have two possible values just like classical bits, but can also support any superposition of those two values. Two energy states in the ion are chosen to represent these two values. Additionally, multiple qubits can be entangled together, which enables the huge speed improvement these systems can achieve.

Although there are many systems under investigation as potential quantum computing technologies, I am only going to seriously discuss the possibilities of trappied ion quantum computers. In order to guide our discussion of how trapped ions represent a possible technology for implementing quantum computation, I will follow the venerable DiVincenzo criteria [**?**]. These criteria were proposed by David DiVincenzo in 2000, and describe the basic requirements for a feasible quantum computing architecture. They place limits on both the chosen qubits and the technologies that isolate and interact with them.

1. A scalable physical system with well characterized qubits

The first criteria is unfortunately the one that is most difficult to realize with a trapped ion system. The qubits themselves, represented by long lived internal energy states of the ions, are certainly well characterized. However, the physical system required to trap the ions and generate entanglement between them has proven difficult to scale to large numbers of ions. Current state of the art systems can simultaneously entangle 14 qubits [**?**], which is already technically very challenging and still of limited use computationally. The focus of the rest of this thesis will be on one proposal for scaling ion trap systems up to useful number of qubits.

2. The ability to initialize the state of the qubits to a simple fiducial state, such as $|000...\rangle$

This ability is easily realized in trapped ions by tuning the polarization or frequency of a group of lasers to drive transitions from all but one accessible long-lived state. The exact details depend on the species being trapped, but are usually very straightforward. Once these transitions are addressed the population will be pumped to the non-addressed long-

lived state by decay from the excited states. From this optically pumped state the qubit can be transferred to whatever state represents $|0\rangle$ in the proposed computation scheme. In practice, only a few lasers are often necessary to realize this procedure and the desired state can be initialized with fidelities easily greater than 99%.

3. Long relevant decoherence times, much longer than the gate operation time

Once again the exact details of the implementation depend on the chosen atomic species and isotope, but there are usually several possible long lived states in a given species that could serve as qubits. In particular, in species with odd nuclear spin there are first order magnetic field insensitive ground state levels with coherence times easily reaching several seconds [**?**, **?**]. There are even energy levels separated by ir and visible optical transition frequencies that have similar decoherence times. These time scales compare very favorably with gate operation times between 1 μs and 10 μs.

4. A universal set of quantum gates

In this context, a universal set of gates refers to a set of operations that can be performed on the qubits in order to realize any unitary operator. In practice, the necessary set can be relatively small and involve only a few single qubit rotations and an entangling operation between qubits. These kinds of operations are easily accomplished using external electric and magnetic fields. The rotations can be accomplished with near-resonant radiation at the qubit energy. The Coulomb interaction between trapped ions provides a strong coupling between their motional energy states that can be used to perform entangling operations. Fidelities for these operations can be very high, and gate times can be very short [**?**].

5. A qubit-specific measurement capability

Ions that can be trapped usually have a strong, optical transition that can scatter millions of photons per second. By manipulating the internal state of the ions to allow or disallow such a transition, the ions state can be read out by merely collecting flourescence. Read out times of tens of milliseconds are easily possible, and times as short as 10.5 μs with 99%

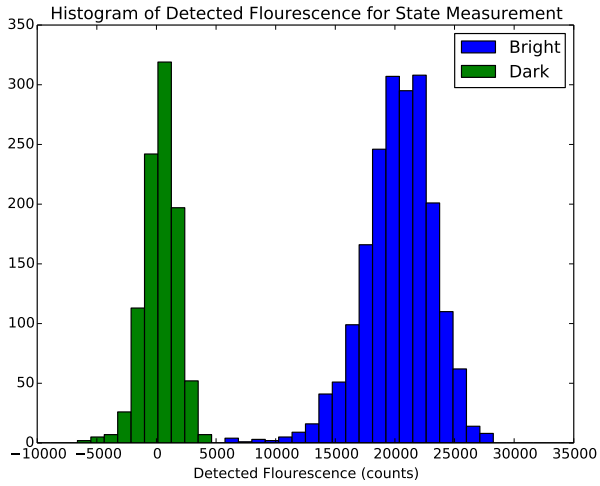

Figure 1.2: Histogram of ion flourescence including "bright" and "dark" ions. The two states can be distinguished with very high probability.

fidelity have been demonstrated [**?**]. This internal state manipulation is often as simple as transferring the ion to a state outside of the decay channels of the driven transition.

1.3 Qubits and Operators

Initialization and readout of trapped ion quantum systems requires easily available lasers and well understood technology as I described above. A universal set of quantum gates can also be engineered, but with some additional complexities. A mathematical approach to the interaction between light and ions will help clarify how to engineer these gates. Once we have chosen our two qubit levels, the state of the system can be described by a wavefunction of the form

$$\Psi(t) = ae^{i\frac{E_0}{\hbar}t}|0\rangle + be^{i\frac{E_1}{\hbar}t}|1\rangle \quad (1.1)$$

$$= \cos(\theta/2)|0\rangle + \sin(\theta/2)e^{i\phi}e^{i\omega t}|1\rangle\,, \quad (1.2)$$

where the second form has dropped an overall phase and made it clear that $|a|^2 + |b|^2 = 1$. We have also defined $\omega = \frac{E_1 - E_0}{\hbar}$. Often such wavefunctions are represented graphically by vectors on the Bloch sphere (see Figure **??**). The $+z$ axis is usually chosen to represent

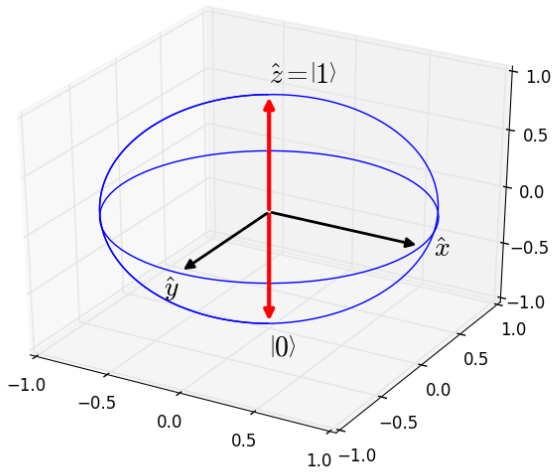

Figure 1.3: Vectors on the Bloch sphere (shown above) can represent any possible qubit state $\Psi = a\,|0\rangle + b\,|1\rangle$. The $\hat{z}$ axis represents $|1\rangle$, while the $-\hat{z}$ axis represents $|0\rangle$.

$|1\rangle$, and the $-z$ axis to represent $|0\rangle$. The polar angle of any arbitrary vector is given by θ, while the azimuthal angle evolves in time and is equal to $\phi + \omega t$. Coherent single-qubit operations can be described as rotations on the Bloch sphere, and their operators can then be written as the familiar Pauli matrices, σ_x, σ_y, and σ_z.

$$\sigma_x = \begin{pmatrix} 0 & 1 \\ 1 & 0 \end{pmatrix} \quad \sigma_y = \begin{pmatrix} 0 & -i \\ i & 0 \end{pmatrix} \quad \sigma_z = \begin{pmatrix} 1 & 0 \\ 0 & -1 \end{pmatrix}$$

Rotations are a convenient basis for describing operations on qubits because all decoherence-free operations will preserve $|a|^2 + |b|^2 = 1$ and will therefore merely rotate states along the surface of the Bloch sphere. To perform these rotations using systems with a strong dipole moment, it is only necessary to use an external electric field. Consider a two level Hamiltonian

$$H = \frac{\hbar}{2}\omega\sigma_z, \tag{1.3}$$

where ω is the angular frequency defined above. We can generally describe coherent inter-

action with an external electric field via the potential

$$V = \left|\vec{\mu} \cdot \vec{E}\right| \cos\left((\omega + \delta)t + \phi_0\right)\sigma_x, \tag{1.4}$$

where $\vec{\mu}$ is the ion dipole moment, $\vec{E}$ is the electric field magnitude and polarization, and δ is the detuning from the the qubit energy spacing of the electric field oscillation.

Consider a qubit system initialized to be in $|0\rangle$. Using time dependent perturbation theory, we can find the time derivatives of the state amplitudes a and b to be

$$\dot{a} = -i\Omega b e^{i\delta t + \phi_0} \tag{1.5}$$

$$\dot{b} = -i\Omega^* a e^{i\delta t + \phi + \phi_0}, \tag{1.6}$$

where we have dropped the quickly oscillating complex amplitudes and defined $\Omega = \frac{\vec{\mu}\cdot\vec{E}}{\hbar}$. For very short interaction times where the amplitudes of the two states do not change we can approximate them as constant and let $a = 1$ and $b = 0$. In this approximation, the population transferred to the excited states is

$$|b|^2 = \Omega^2 t^2 \sin^2 \delta t. \tag{1.7}$$

This equation will be useful for using short pulses to make easy measurements of Ω in later chapters.

The above approximations hold for small population transfers, but in order to analyze the long term behavior we need to simultaneously consider both the excited and ground state occupations. In order to make a geometric connection we can start by considering

$$u = ab^* + a^*b \tag{1.8}$$

$$v = -i(ab^* - a^*b) \tag{1.9}$$

$$w = |b|^2 - |a|^2 \tag{1.10}$$

where u, v, and w are the x, y, and z components of the Bloch sphere representation of $|\Psi\rangle$. Their time derivatives can then be found using Equations **??** and **??** to be

$$\dot{u} = \delta v \tag{1.11}$$

$$\dot{v} = -\delta u + \Omega w \tag{1.12}$$

$$\dot{w} = -\Omega v \tag{1.13}$$

Defining $P = u\hat{x} + v\hat{y} + w\hat{z}$ to be the vector representing Ψ, we can write $\dot{P} = P \times (\Omega\hat{x} + \delta\hat{z})$. This formulation makes it clear that we can coherently control the state of the qubit by controlling the frequency and amplitude of near resonant electric fields. These degrees of freedom choose a vector about which the Bloch sphere representation of the qubit state will process, and choosing the correct time duration allows us to reach any state we desire.

If we are only interested in the probability of measuring $|1\rangle$ after beginning in $|0\rangle$, we can derive the results easily from Equation **??**. The maximum probability to reach $|1\rangle$ can be found by reflecting the $-\hat{z}$ axis across the vector $\vec{W} = \Omega\hat{x} + \delta\hat{z}$, and the rotation speed is determined by the length of W. The transition is driven with probability

$$|b|^2 = \frac{\Omega^2}{W^2} \sin^2(Wt/2) \tag{1.14}$$

where we have defined

$$W^2 = \Omega^2 + \delta^2. \tag{1.15}$$

By applying resonant electric fields we see that we can cause population to oscillate between $|0\rangle$ and $|1\rangle$. Simply controlling the exposure time of the fields to the ion allows us to perform an arbitrary rotation around the $\hat{y}$ axis on the Bloch sphere. Given the strength of these couplings in ions full population transfers can easily be achieved in 1 μs to 10 μs. By controlling the detuning of the field or by allowing some phase evolution between the field and qubit, we can perform rotations about $\hat{z}$. Combining the two we can coherently manipulate single qubits into any desired state.

However, the fundamental speed increases available through quantum computation rely on the ability to generate entanglement between qubits. Without entanglement a quantum computer will not be able to outperform a classical, probabilistic computer. Therefore, we must have at least one operation which can generate entanglement between our qubits. A common choice is called a controlled NOT operation. Its operation can be described by the unitary matrix

$$U_{CNOT} = \begin{pmatrix} 1 & 0 & 0 & 0 \\ 0 & 1 & 0 & 0 \\ 0 & 0 & 0 & 1 \\ 0 & 0 & 1 & 0 \end{pmatrix}. \tag{1.16}$$

The controlled qubit's state is flipped if the controlling qubit is set, and otherwise is not changed.

While single qubit operations are relatively easily engineered, implementing entangling operations is signifcantly more difficult. The method used to implement them is dependent on the interaction that cen be engineered between the qubits themselves. In trapped ion systems, N ions that are confined in the same trap share $3N$ quantum harmonic oscillator modes of motion coupled via Coulomb forces. These harmonic oscillator states are used as intermediate states to allow communication between the qubits. A number of methods for generating entanglement between ions have been proposed including the Cirac-Zoller gate [**?**], the Mølmer-Sørensen gate [**?**], and the García-Ripoll gate [**?**]. The García-Ripoll gate has the most desirable properties including being completely insensitive to the ions motional energy and having a total gate time that can be much quicker than the time scale of the motion of the ions. However, the optical setup to efficiently implement it is very complicated, and we will instead use the Mølmer-Sørensen gate for the moment.

The Mølmer-Sørensen gate is a two qubit entangling gate that uses these motional modes and is tolerant to finite temperature in them. For a normal mode with angular frequency ω_x and a qubit angular frequency ω, the two ions are exposed to an two external fields with angular frequencies $\omega \pm (\omega_x + \delta)$. These fields excite a virtual phonon into the motional mode and then remove it. The result of the pulse sequence is independent of the number of quanta in the mode, but the two ions are linked via the motional mode and must coherently transition together. The action of this pulse sequence on two qubit states of our qubit levels, $|0\rangle$ and $|1\rangle$, can be described by

$$|00\rangle \rightarrow \cos\left(\frac{\Omega' t}{2}\right)|00\rangle + i\sin\left(\frac{\Omega' t}{2}\right)|11\rangle \tag{1.17}$$

$$|11\rangle \rightarrow \cos\left(\frac{\Omega' t}{2}\right)|11\rangle + i\sin\left(\frac{\Omega' t}{2}\right)|00\rangle \tag{1.18}$$

$$|01\rangle \rightarrow \cos\left(\frac{\Omega' t}{2}\right)|01\rangle - i\sin\left(\frac{\Omega' t}{2}\right)|10\rangle \tag{1.19}$$

$$|10\rangle \rightarrow \cos\left(\frac{\Omega' t}{2}\right)|10\rangle - i\sin\left(\frac{\Omega' t}{2}\right)|01\rangle \tag{1.20}$$

where we have defined

$$\Omega' = \frac{(\Omega\eta)^2}{\delta - \omega_x}, \tag{1.21}$$

and Ω is the coupling strength of the field to the qubit transition while η is the Lamb-Dicke parameter that describes the coupling strength between the field's momentum and the ion's motional states. Since this transition is indpendent of the motional energy level of the ion n, it can be driven with relatively high temperatures that can easily be reached with simple laser cooling techniques. The entanglement is even robust against ion heating during the transition and only requires that the ion be cold enough to satisy $\eta^2 n \ll 1$. The Mølmer-Sørensen gate implements an entangling operation, but it is not the easily described CNOT operation from above. However, by performing single qubit rotations before and after this entangling operation, CNOT gates can be engineered.

Implementing a quantum algorithm can be thought of as implenting a complicated unitary matrix on a number of input and ancillary qubits. However, it is easiest experimentally to perform and optimize a small number of single qubit and CNOT gates. Fortunately, the Solovay-Kitaev algorithm allows us to approximate the quantum algorithm we want to perform using a universal set of simple gates. This algorithm allows us to construct an appoximation with error at most ϵ to any unitary matrix using a number of simple gates that scales as $\log^2(1/\epsilon)$. The approximation can be found efficiently on a classical computer before the algorithm is implemented on a quantum device. For this reason, we can concern ourselves with only implementing relatively simple quantum operations, with the promise that by performing many of these gates we can approximate any algorithm. The only problem with this procedure is the accumulation of errors by performing hundreds or thousands of these simple gates. For complicated quantum algorithms, quantum error correction will probably be necessary to stop this propagation of error and maintain the fidelity of the approximation to the algorithm in question. Quantum error correction was first conceived of by Shor and requires more ancilla qubits for each computational qubit and more simple gates for each operation, but promises a higher total fidelity at the end of the algorithm[**?**]. The techniques have been adpated to many different quantum computing proposals including new, scalable architectures for trapped ions[**?**].

All of the requirements for quantum computation have been demonstrated with simple ion trapping systems using readily available technology. The difficulty remains in scaling the number of communicating trapped ions to a sufficiently large number to outperform classical computers. The number of required ions is not the billions it would take to compete with the number of bits in a classical computer, but instead only a few hundred because of the incredibly efficient quantum algorithms that are available for some difficult problems. In Chapter **??**, I will discuss our strategies for reaching these numbers of communicating ions.

Chapter 2

SCALABLE ION TRAP QUANTUM COMPUTATION

Hopefully, I have convinced you by now that trapped ions offer the potential to easily realize the building blocks of a quantum computer. The difficulty in performing useful quantum computing tasks with them is then relatively easily reduced to the problem of having a sufficient number of communicating qubits available. A single ion trap can easily confine ten ions, but as more ions are loaded into the trap difficulties begin to arise. It becomes increasingly difficult to stably trap large chains, and once trapped it is more difficult to spatially address individual ions with lasers and to address individual entangling transitions between ions in frequency. The motional amplitude per ion in each mode is reduced and the additional motional modes of the trap contribute to decoherence through off-resonant processes.

2.1 MUSIQC Architecture

To address these issues a collaboration of ion trappers proposed a new ion trapping architecture that works towards scalability in three ways. The architecture is known as the Modular Universal Scalable Ion-Trap Quantum Computer (MUSIQC). The first increase in scalability is to implement additional voltage degrees of freedom to improve our control of dc electric fields in ion traps. This technology will enable us to trap additional ions in a single trapping region and to form additional trapping regions in each vacuum chamber. In order to easily address and image ions from outside of the vacuum chamber, it is far preferrable to crystallize them in a linear chain. Therefore, their axial confining strength must be kept weaker than their radial confining strength. The difficulty arises that, as more ions are loaded into the same trap, the ions at the outer ends of the chain provide additional axial confinement to the center ions. The result of which is that trapping increasing numbers of ions in a linear chain requires increasing amounts of radial strength. Especially for heavier

ions species, increasing radial strength can become difficult quickly.

In order to correct for this effect it is desirable to lower the axial confinement that the center ions experience without compromising the confinement of the entire chain. Since ions are very sensitive to electric fields, it is easy to add additional controls to their confinement just by adding more dc control electrodes. In order to have many small control electrodes, ion traps that are made using standard micromanufacturing techniques have been developed. These techniques have been used in the condensed matter community for decades and transfer very well to the manufacture of small ion traps. Using these additional trap degree of freedom we expect to be able to trap ≈ 20 ions in a trapping region.

Using these additional dc voltage controls, it is also possible to generate and control multiple trapping regions inside the same vacuum chamber. In fact, generating multiple trapping locations, and separating ions from and merging ions into these regions has already been demonstrated [**?**, **?**]. While entangling operations can only occur between ions in the same trapping region, ions carrying information can be shuttled between different regions without decoherence [**?**]. The separation and merging operations using our current dc control systems takes several milliseconds, and the operation might be complicated depending on how many ions need to be reordered to transfer the desired information.

Using these techniques it is possible to store hundreds of ions inside a single vacuum chamber. While this would be a very impressive technical demonstration, it would not be a modular system and additional scalability would be difficult. Also, adding more trapping regions to each vacuum chamber increases the difficulty of shuttling ions between them. All of the fields applied to the ions need to be carefully focused and directed to avoid interacting with the many other ions inside the ≈ 1 cm diameter micro-trap. Applying rf and microwave control fields to single ions in such systems would be very difficult because of their wavelengths, which is unfortunate because many desirable qubit levels are separated by these frequencies. While none of these difficulties are insurmountable, a separate, additional method of scaling our system will almost certainly prove useful.

The second way that we propose to work towards scalability is by transferring entanglement between separate vacuum chambers. This brings us to another advantage of working with ions. Given an appropriate choice of qubit, it is very easy to generate entanglement

between ions and single photons. The resulting state of the emitting ion can be encoded into the frequency and polarization of the emitted photon. The problem of coupling quantum information in ions in multiple vacuum chambers is then reduced to the problem of coupling photons between the chambers.

Coupling photons together is a problem that has already been almost entirely solved. Optical fiber technology is available that will transfer photons from ions with reasonable loss rates. Any necessary operations on the photons polarization or frequency can be accomplished using optical fiber tools. The only remaining difficulty is interconnecting the fibers of any desired pair of ion traps. This last task can be accomplished using a custom microelectromechanical system (MEMS) of mirrors to redirect light from an input array of fibers to any desired output fibers which has already been demonstrated [**?**].

For reasons discussed in the next section, this photonic information transfer will be significantly slower than the timescale of other operations in the trap. Quantum gates between ions in the same trap can usually be performed at rates of $\approx$ 100 kHz to 1 MHz. Shuttling ions containing information between separate trapping regions can be accomplished at a rate of $\approx$ 1 kHz - 10 kHz. Transferring quantum information between remote ions in separate vacuum chambers currently takes $\approx$ 1 s to 10 s, but we believe that we can reduce this time to $\approx$ 10 ms.

Nevertheless, quantum algorithms will be possible using this architecture. Analysis has shown that the MUSIQC architecture compares favorably with other commonly suggested scalable quantum computer architectures [**?**]. The slower remote entanglement step also does not preclude the implementation of quantum error correction. Quantum error correction is a complicated scheme by which a single qubit value is encoded into multiple physical qubits so that simple errors in the quantum gates can be avoided. It is expected to be difficult to perform large quantum algorithms without error correction because it is difficult to engineer quantum gates with high enough fidelity that large computations do not often fail.

The third technique we have been developing is the use of multiple ion species in the same trapping region. This idea developed out of necessity from the difficulty in cooling ions and performing quantum operations with the same ion species.

2.2 Remote Entanglement

The proposed MUSIQC architecture involves multiple separate vacuum chambers with lasers for cooling and quantum operations. Each vacuum chamber features a few locations that are optically coupled to a single mode optical fiber. Light from different ions can then be brought to a MEMS-based mirror switching system, which can combine light from different fibers reliably and repeatably.

The one complication to this scheme is the difficulty in collecting large fractions of the photons that an ion emits and focusing those photons onto other ions. In order to generate entanglement it is necessary to be able to detect a single photon emitted by an ion. A straightforward ion trap that was not designed with this feature in mind will usually collect and image approximately 2% of the available ion flourescence. As a result the probability of successfully managing to entangle two ions in distant traps in a single trial will be vanishingly small. Attempting the entanglement and hoping that it worked is not a realistic possibility. Fortunately, there is a protocol by which it can be determined whether the entanglement process was successful without performing a measurement that would destroy the entanglement.

Instead of attempting to directly couple photons carrying information from one ion onto another ion, we will separately collect such photons from both ions simultaneously. For example, considering vacuum chambers A and B, photon quantum states $|H\rangle$ and $|V\rangle$, and ion quantum states $|\uparrow\rangle$ and $|\downarrow\rangle$ we will generate the states

$$|\Psi\rangle = \sum_{i=A,B} \frac{1}{\sqrt{2}} \left(|H\rangle_i |\uparrow\rangle_i + |V\rangle_i |\downarrow\rangle_i\right). \tag{2.1}$$

The photon states need to be some distinguishable photon states maximally entangled with the ion states. Polarization states can be used easily or frequency states can be used if the frequency separation is larger than the linewidth of the transition. We can then overlap the photon spatial modes on a 50-50 beamsplitter at some other location. When single photon detectors placed at both output ports of the beamsplitter are simultaneously triggered that will correspond to measuring the photon state as $\frac{1}{\sqrt{2}} \left(|H\rangle_A |V\rangle_B + |V\rangle_A |H\rangle_B\right)$. We can determine the resulting state of the ion by projecting that state onto this measurement.

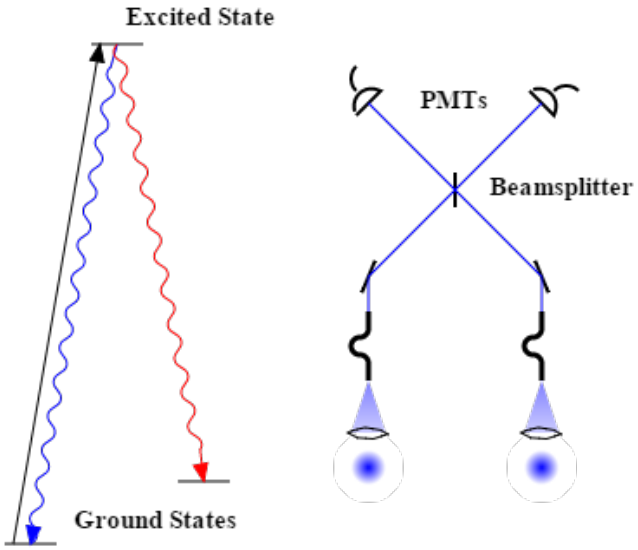

Figure 2.1: Diagram of the remote ion-ion entanglment experiment. An ion is excited to a state with two possible photon decay paths (left). The photons are collected and spatially overlapped before being detected on two PMTs (right). The overlap removes the which-path information from the system before the detection and leaves the ions entangled.

The ions are left in the state

$$|\Psi\rangle = \frac{1}{\sqrt{2}} \left(|\uparrow\rangle_A |\downarrow\rangle_B + |\downarrow\rangle_A + |\uparrow\rangle_B \right) \tag{2.2}$$

which is a maximally entangled state of the ion qubits. This procedure is usually destructive of the ions initial state, but remotely entangled qubits can be prepared in advance and used a resource during the computation.

In any given attempt an entangled ion-photon pair can be generated with probability P given by,

$$P = P_{\text{exc}} f \eta \frac{\Omega}{4\pi} f_{\text{gate}} T \tag{2.3}$$

where P_{exc} is the probabilty of driving the transition to the excited state (≈ 0.2 in our current experimental setup), f is the branching ratio back to the initial state if other decays

are possible (≈ 0.75), η is the quantum efficiency of the single photon detector (≈ 0.2), Ω is the solid angle for the collection optics ($\approx 0.02 * 4\pi$), f_{gate} is the fraction of emitted photons in our detection window (≈ 0.8), and T accounts for other losses including transmission through all other optics (≈ 0.3). These factors limit us to generating an entangled pair only every 400 ms given our 17 kHz repetition rate[**?**].

Generating an entangled ion-ion pair requires the simultaneous generation of two ion-photon pairs which means that it only succeeds with probably proportional to P^2. The photons must also be transmitted through a length of optical fiber, have their spatial modes overlapped, and be in a correct state to allow the heralded entanglement scheme to occur, but these factors are insignificant or unavoidable. The largest achievable gains in our apparatus would be to P_{exc} which can easily be increased to unity, and Ω which can be increased by a factor of 5 to 10. The MUSIQC collaborators are exploring a number of possible methods to improve Ω including in vacuum cavities [**?**] and diffractive optics [**?**]. Gang Shu and CK Chou have designed and built an ion trap inside of a parabolic mirror which can be used to collect $\geq 40\%$ of an ion's flourescence[**?**], and we are working to implement this experiment in that system.

Using currently available technology a remote ion-ion entanglement rate of ≈ 10 Hz to 100 Hz is feasible and we are working towards achieving that goal.

2.3 Mixed Ion Species

Unfortunately, as the implementation of this scheme proceeded, field crosstalk was still a problematic issue. The generation of remote entangled ion pairs still requires the application of resonant laser beams on strong transitions. Even with ion separations of 10 microns, well focused lasers can still scatter hundreds of photons per second from neighboring ions. Scattering any photon will completely destroy the quantum information that might have previously been held in the ion, and can quickly disrupt an entire calculation. The determination was eventually made that we needed to take measures to avoid this problem.

The method chosen to minimize the field crosstalk issue was to use separate ion species for quantum computation and the remote entanglement generation. This choice cements the idea of remote entangled pairs as a computational resource. One ion species can be

dedicated to generating many entangled pairs that can be transferred into the computation by quantum teleporting the entanglement onto the computational ion species. Only the computational ion species will store quantum information for any significant period of time or perform any calculations with it. Previous work towards a similar mixed ion species system has been done with small numbers of ions already [**?**].

Another advantage of adapting this scheme is that there are now many ions motionally coupled to the computational ions, but with well separated transition frequencies. Laser cooling can be performed continuously on the remote entanglement species with a negligible chance of scattering a photon from the computational ions. Since the two species are motionally coupled, it should be possible to keep the entire chain of ions cold without affecting ongoing quantum algorithms. By using quantum gates that are insensitive to small motional occupation numbers and electromagnetically-induced-transparency cooling [**?**, **?**] it may even be possible to avoid ever having to laser cool the computational ions. This would allow quantum algorithms to continue running until qubit begins to decohere instead of being forced to stop by heating issues as is often the case. The use of the Mølmer-Sørensen gate discussed in Chapter **??** is also helpful here because of its resistance to decoherence even when performed at finite ion temperatures and during ion heating.

The added difficulty in only laser cooling one species is that different ion species obviously have different masses, which causes each normal mode of the chain to couple more strongly to one ion species than the other. For large mass differences, this imbalance can make it impossible to cool one ion species using the other. Each mode will have eigenvector components of order one with one ion species and all of its eigenvector components with the other ion species may be ≤ 0.01 or even less. The result is that even with large amounts of energy in this mode, the ion species being laser cooled may have very little motion.

It is hoped that by choosing ion species with small mass differences and by exploring other degrees of freedom, this cooling scheme may be possible. These other degrees of freedom include number and arrangement of the cooling ions and overall trap strengths and anharmonicities. After going through our ion trapping, cooling, initialization, and readout procedures in more detail in Chapters **??** and **??**, I will explore these ideas further.

The two ion species that will be used for the MUSIQC program are ytterbium and

barium. Ytterbium-171 has a pair of ground state levels with excellent insensitivty to magnetic fields. These levels have very long coherence times and the state of the ion can be determined using a simple optical setup. Barium has the advantage of having a strong transition at 493 nm, which is a long wavelength transition among ion species that can be laser cooled. This wavelength is transmitted through fibers easier than more ultraviolet transitions which will improve the rate at which remote entangled pairs can be generated. Further the two species are relatively close in mass, which should help to increase their motional coupling.

Part II

TRAPPING BARIUM AND YTTERBIUM IONS

Chapter 3

LINEAR RF AND SURFACE TRAPS

Basic electrostatics requires that in free space the electric potential ϕ obey

$$\nabla^2\phi = 0 \tag{3.1}$$

and therefore it is impossible to have $\partial_x^2\phi > 0$, $\partial_y^2\phi > 0$, and $\partial_z^2\phi > 0$ at the same point in space, which is the condition for having a stable trap in three dimensions for a positively charged particle. The best possibility with electrostatics is to form a trap in two dimensions, but the third axis will always be an unstable equilibrium point.

Therefore to stably confine a charged particle we have to use either static magnetic fields or time-varying electric fields. Both of these possibilities are used in modern labs, but working with magnetostatics in Penning traps requires that the ions precess about the magnetic field axis which makes performing quantum operations on them more difficult. All control lasers and readout must be continuously corrected for the rotation [**?**, **?**]. These traps are often used for precision measurements. Instead, most quantum information efforts with trapped ions use linear rf traps, which use radio frequency and dc electric fields to generate stable trapping [**?**]. Linear rf traps allow stationary confinement of any charged particle.

In order to more rapidly evaluate different ion trap designs, we have been working on two separate traps in different vacuum chambers. Power from all of the necessary ionization and cooling lasers is split between the two traps. Both chambers were originally designed to hold microfabricated surface traps, but one has been converted to hold a standard macroscopic linear rf trap in order to more easily test new quantum operations.

3.1 Linear RF Traps

The easiest linear rf trap geometry to understand features four long rods arranged in a square with their long axis along z (see Figure **??**). Radio frequency voltage is applied to

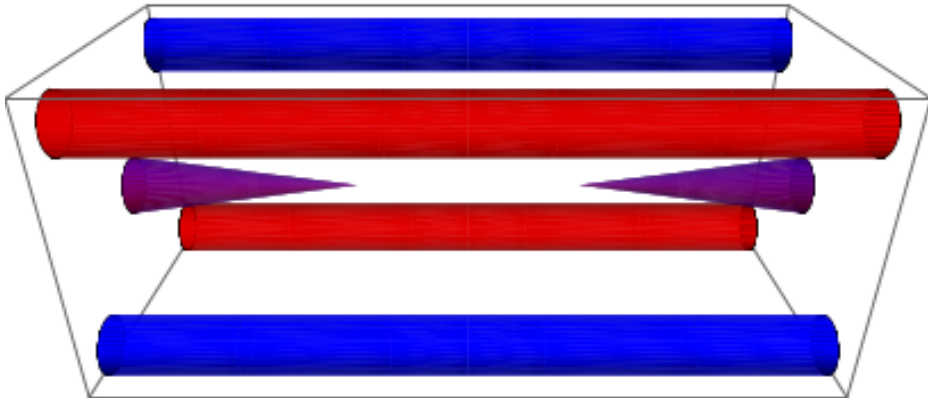

Figure 3.1: Schematic drawing of a linear rf trap showing rf (red) and ground (blue) rods, as well as high voltage dc needles (purple).

two rods in opposite corners (red) and the other two rods are grounded (blue). The rods provide radial confinement for the ions, and axial confinement is then provided by applying high voltage dc to two electrodes centered inbetween the rods at opposite ends (purple).

At the center of the trap the rods form a radial oscillating quadrupole electric field that is a function of the frequency of the applied rf, Ω.

$$\Psi_{\mathrm{rf}} = \kappa_{\mathrm{rf}} V_{\mathrm{rf}} \cos(\Omega t) \left(x^2 - y^2\right) \tag{3.2}$$

while the dc electrodes form a stable trap in the z (axial) direction, and an unstable equilibrium position in x and y.

$$\Psi_{\mathrm{dc}} = \kappa_{\mathrm{dc}} V_{\mathrm{dc}} \left(z^2 - \frac{1}{2}\left(x^2 + y^2\right)\right) \tag{3.3}$$

The axial confinement is therefore straightforward and follows directly from just the dc potential.

The resulting axial secular frequency can easily be derived from Equation **??** and is $\omega_z = \sqrt{2\kappa_{\mathrm{dc}} V_{\mathrm{dc}} q/m}$ for an ion of charge q and mass m. The radial equations of motion can be converted to the standard form

$$\frac{d^2x}{d\xi^2} + (a_x + 2q_x \cos(2\xi))x = 0 \tag{3.4}$$

with the definitions

$$\xi = \Omega t/2 \tag{3.5}$$

$$a_x = \frac{4q\kappa_{\rm dc}V_{\rm dc}}{m\Omega^2} \tag{3.6}$$

$$q_x = \frac{2qV_{\rm rf}}{\Omega^2 m}. \tag{3.7}$$

Typically in experimental conditions we will have $a_x < q_x^2 \ll 1$, which is a stable solution of the Mathieu equation. The motion of the ion under these approximations can be written as

$$x(t) = A_x \cos(\omega_x t + \phi_x)\left(1 + \frac{q_x}{2}\cos(\Omega t)\right). \tag{3.8}$$

The radial secular frequencies, ω_x, correspond to the restoring force the ion feels and are equal to

$$\omega_x = \frac{\Omega}{2}\sqrt{\frac{a_x + q_x^2/2}{1 - 3q_x^2/8}}. \tag{3.9}$$

The A_x parameter is an amplitude set by the initial conditions of the ion. There is still some residual motion of the ion at the frequency of the applied rf, Ω. All of the above arguments carry through for both radial directions although I've only been discussing x. However, it is undesirable to have the radial frequncies be extremely close together because of the resulting low frequency beat note them that makes the ions sensitive to low frequency electric field noise. Therefore, the ω_x and ω_y are usually separated either though geometry or by applying a radially symmetry breaking dc field.

In Figure **??**, a solution to the Mathieu equation given a starting location near the trap center is shown. The ion is confined radially with a restoring frequency corresponding to the slower oscillations seen above, while some faster oscillations that come directly from the applied rf frequency also perturb the ions' motion. These fast oscillations are known as trap micromotion and are minimized as much as possible. They lead to micromotion sidebands on all lasers applied to the ion and increase ion heating when ions are moved by changing dc electrode voltages. The micromotion is induced when the ions are pushed off the quadrupole null by stray dc electric fields.

In addition the amplitude of the trap micromotion as a function of stray field can also be found by analyzing the Mathieu equation. It is usually parameterized by a value $\beta =$.

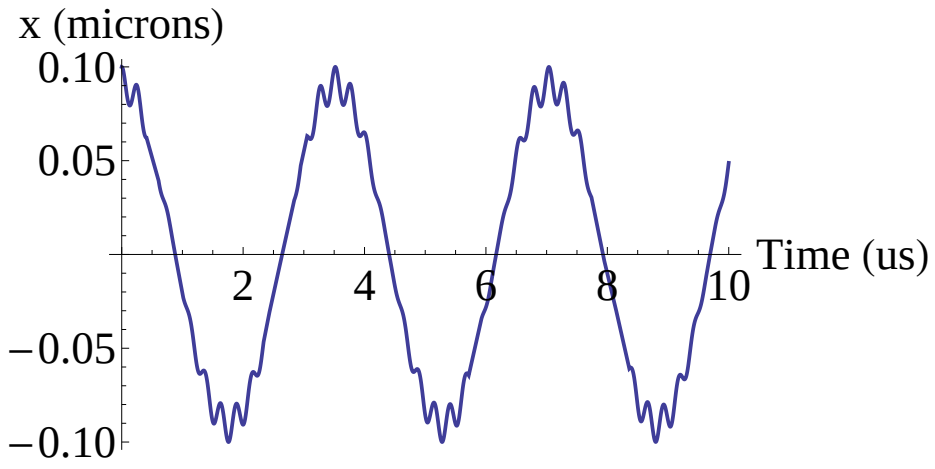

Figure 3.2: Solution to the Mattheiu equation for a possible linear rf trap geometry showing secular motion and driven micromotion in one radial direction.

By cancelling out the stray field as much as possible the micromotion amplitude can be reduced.

When we are working with standard macroscopic linear rf traps we have used a design exactly as pictured in Figure **??**. The trap is formed by four 0.017 in diameter tungsten rods separated by approximately 800 microns. The rods are held in place at either end of the trap by an alumina spacer. In order to provide axial confinement two tungsten needles were created by electrochemically etching a fine point onto tungsten rods []. These needles are also inserted into the alumina spacers and everything is secured with a UHV-compatible quick-drying cement.

The rods and needles are connected to an 8-pin vacuum feedthrough. High voltage rf to generate the trapping potential is created using a helical can resonator. Two long pieces of copper are wound into a two-strand copper helix and held in the center of a large copper can. One end of each copper piece is connected to an rf ground and the other is connected to the vacuum feedthrough. Rf is coupled into the resonator using a small induction coil whose shape and length can be manipulated to match the load to a standard rf amplifier.

The ground electrodes and the end of the helix coils after the rf filter are connected to

dc voltage sources. By adjusting the dc voltage of these four rods we can control the radial dc field in the trap. These degrees of freedom allow us to cancel out stray field that may be present in the trap as well as break the radial symmetry of the trap to separate the two radial secular frequencies.

Although the effects of the rf are easiest to see in this type of linear rf trap geometry, many different rf and dc electrode geometries are possible. The only requirements for this kind of trapping to work are an oscillating quadrupole field overlapped with dc confinement in the other directions. A particularly simple electrode geometry is applying rf to a metal ring with dc electrodes above and below it. Another geometry used in my group applies rf to a large parabolic mirror with a grounded metal needle inside of it [**?**]. The ion's position can be manipulated by moving the needle, and by positioning it at the focus of the parabolic mirror very large fractions of the light emitted by the ion can be collected.

3.2 Surface Traps

A favorable geometry for working towards scalable quantum computing is called a surface electrode trap. In this geometry, all of the electrodes are place in a single plane. Surface electrode traps have several advantges over standard millimeter scale linear rf traps including repeatable manufacturing processes and many separately controllable dc electrodes. These electrodes allow the creation of separate trapping regions as well as shuttling between the regions and splitting and merging ions into them. Many groups have been developing the techniques to design and manufacture these traps [**?**, **?**, **?**].

Georgia Tech Research Institute and Sandia National Lab have provided us with surface traps for evaluation. The MUSIQC collaboration has been exploring a number of possible features that can be engineered into surface traps including regions of hight optical access to allow tightly focused lasers, regions with optical cavities to increase ion flourescence collection, and junctions between linear trapping regions that allow chains with different ion species composition and ordering to be organized. In order to be able to evaluate different traps quickly we have designed an implemented a vacuum chamber that allows for quick trap replacement.

The surface electrode traps we receive are wirebonded onto a CPGA-100 carrier. This

carrier slots into a UHV-compatible Zero Insertion Force (ZIF) socket in the center of our vacuum chamber. The ZIF socket connects to a custom PCB that can host additional filtering for the dc voltages that will be applied to the trap if necessary. The PCB also routes the connections from the socket to four 25 pin D-Sub connectors that are connected through a vacuum feedthrough to our control electronics. The neutral atom oven mount below the PCB. The bottom flange of the vacuum chamber can be removed to replace the oven, and the top flange can be removed to replace the trap. This system has been cycled from atmospheric pressure to pressures below 5×10^{-11} more than ten times often in a week or less.

The electric fields at the trapping location in surface traps are often calculated using the Boundary Element Method (BEM). All of the surfaces in the trap are subdivided into small triangles or quadrilaterals and a surface charge degree of freedom is placed at each vertex of this mesh. The actual surface charge is assumed to be the linear interpolation of these points. This step reduces the problem from one large integral to the sum of a large number of integral that depend linearly on these vertex surface charges. In other words the problem of solving for ϕ is changed from

$$\phi(x) = \int_{\{S\}} \frac{\sigma(x')}{4\pi \left|x - x'\right|} dx' \text{to} \tag{3.10}$$

$$\phi(x_i) = \sum_{S_k = x_q, x_r, x_s} \int_0^1 \int_0^v \frac{(1-u-v)\sigma(x_q) + u\sigma(x_r) + v\sigma(x_s)}{4\pi \left|x(u,v) - x_i\right|} \left| \frac{\partial x}{\partial (u,v)} \right| dudv, \tag{3.11}$$

where σ is the surface charge density and u and v are a paremtrization of the small triangular surface S_k defined by the three vertices x_q, x_r and x_s. The desired solution is then a set of $\sigma(x_i)$ given a desired set of voltages on each surface $\phi(x_i)$.

The problem of solving for these vertex surface charges can then be reduced to linear algebra by computing these integrals without the σ parameter. Then given the desired voltages on each surface the resulting surface charge distribution can be calculated by standard linear algebra techniques. We have developed software that performs the integration using Gaussian quadrature, and inverts the generated matrix using the open source PETSc package.

Usually in order to be able to quickly analyze voltage solutions the electric field of each

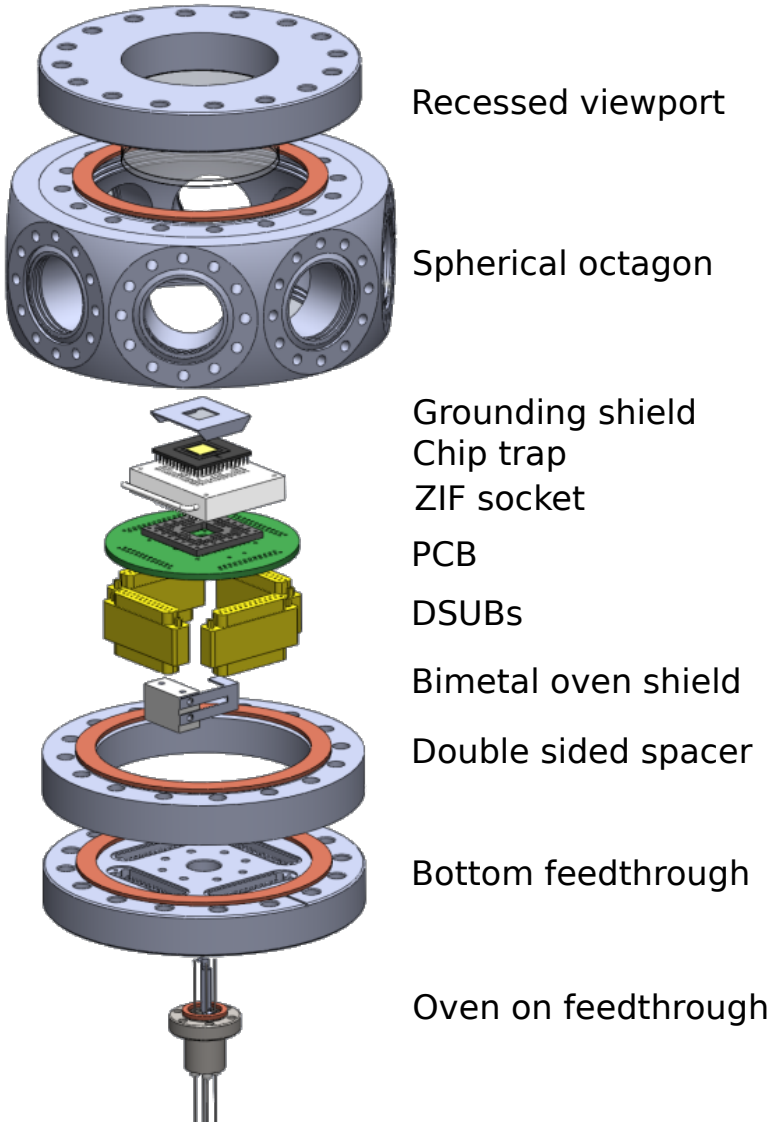

Figure 3.3: Diagram of vacuum chamber with integrated systems to facilitate the easy replacement of surface electrode traps.

electrode is solved individually. Every electrode is set to 0 V except for one which is assigned some nominal value like 1 V. The total electric field for a set of voltages can then be found by scaling and adding these results for each electrode. The radial trapping potential is analyzed by performing the same analysis for the rf electrodes and the calculating the electric field from this analysis. The radial behavior of the ion can be described by an rf pseudopotential approximation

$$\phi_{\text{pseudo}} = \frac{e}{4m\omega^2} \left|\nabla \vec{E}\right|^2 \tag{3.12}$$

where $\vec{E}$ is the electric field vector, e is the electron charge, m is the ion mass, and ω is the frequency of the applied rf voltage. The secular motion of the ion is described by this potential under the same approximations that we made before, but micromotion is not taken into account.

Multidimensional functional minization is then used to solve for voltage solutions with desired trap strengths or locations. Ions can be shuttled axially by solving for voltage solutions that generate a trap every few microns along the region of itnerest. Applying these solutions in order at some sufficiently high fixed speed will shuttle the ion at roughly constant velocity.

Once a trapping potential has been calculated, it must be applied to the dc electrodes. The current generation of traps have up to 96 dc electrodes that must be independently controlled. After evaluating potential solutions including many National Instruments cards in PCI chassis and a hundred separate high precision DAC chips, I decided to implement a solution using a few many-channel DAC chips. The AD5372 is an Analog Devices chip that contains 32 independent DACs with 16-bit precision and 20 V output range. The latter two specifications are sufficient for our needs and with 32 channels three chips suffice to control any surface electrode trap.

The disadvantage of using a many-channel chip is that it is not possible to update the voltages of all of the electrodes simultaneously. Each chip supports a serial interface at 50 MHz and a minimum time between channel updates of 600 ns. Often it is necessary to update many electrodes near each other for example to slightly adjust the potential near an ion to change its stray field correction or to begin a shuttling operation. Therefore, it's

often necessary to send a sequence of $\approx$ 8 to 10 sequential writes to a single chip for a single step in a shuttling solution. The overall update rate for a single step in a shuttling solution is therefore usually limited to 10 kHz to 100 kHz. The AD5372 does include the functionality to buffer all of these updates into its registers and then present the voltages simultaneously to the ion trap. The potential the ion sees is never in an intermediate state and always corresponds to one of the potentials in the solution file even though the updates are communicated serially to the DAC board.

Communication with the DAC chips is accomplished through their serial interface using a custom FPGA software solution implemented on an Altera DE2-115 FPGA development board. This board features 512 KB of SRAM volatile memory and a DM9000a ethernet controller. In order to shuttle the ion, the lab computer loads the shuttling solution from files and transmits it via UDP packets to the DM9000a ethernet controller. The FPGA board stores each solution step in its SRAM memory and confirms its receipt to the lab computer. Once the solution has been loaded it can be played from any desired step to any other at the maximum update rate of the DAC chips. Since each step could take a different number of updates and it is desirable to maintain the same time period between steps in the shuttling solution file the FPGA will automatically generate delays if necessary between solution steps.

Using this system we have successfully trapped in two different surface electrode traps and have demonstrated shuttling ions. In order to work on ions at different positions along the axis we have also developed computer controlled systems for positioning the cooling lasers and imaging systems. We currently shift the position of the cooling lasers using a mirror with a piezoelectric control system. A custom dc-dc amplifier transforms voltages from an ADC output from a microcontroller into a high voltage input for the piezo mirror. The microcontroller communicates with the experimental control computer over a serial interface, and it can be program to any desired voltage or to sweep over multiple voltages spending a designated amount of time at each voltage. This second mode is useful for working on multiple trapping regions at the same time.

In this chapter we have developed all of the technology we will need to trap ions for the rest of this work. Macroscopic linear rf traps are useful for easily evaluating new technologies

because of their lower heating rates and easier optical access. Surface traps will enable us to work with larger numbers of ions and to work efficiently with multiple ion species. The next two pieces of setup we need are the ionization lasers and the cooling lasers that will create our ions and maintain their low temperatures. I will discuss these in the next chapter.

Chapter 4

WORKING WITH BARIUM AND YTTERBIUM

The two ion species that were chosen to load into these traps as part of our computer architecture were barium and ytterbium. These elements have several advantages for building a quantum computer using our architecture which will be discussed in this chapter. Ytterbium will be used to implement the actual quantum computation, while barium will be used to generate remotely entangled ion pairs between ion traps and cool both species.

4.1 Ionization

Before any of the trapping technology discussed in the previous section will work we need a source of ions. The atoms to be ionized are generated by heating a small alumina oven inside the vacuum chamber. The oven is loaded with small pieces cut from a barium or ytterbium sample before the chamber is sealed. It is wrapped with small diameter tungsten wire which is then connected to a vacuum feedthrough. By running currents between 1-2 A (depending on the length of the wire and its contact with the oven) the oven can be heated to a sufficient temperature to emit a usable flux of the neutral atom. The flux from the oven is difficult to measure directly, but very reasonable trapping rates of a few ions per minute can be achieved with these currents. Ionization is accomplished by applying lasers energetic enough to strip the outer electron from the atom, often using intermediate states of the neutral atom to provide isotope selectivity or increase the wavelength of the necessary beams.

Barium is an alkaline earth metal which makes the atomic structure of its ion easy to analyze. The energy structure can be almost entirely understood by considering the single remaining valence electron (once the second valence electron is removed by ionization) interacting with the nucleus electrically shielded by the remaining electrons. It has two low energy D orbital angular momentum states with very long lifetimes.

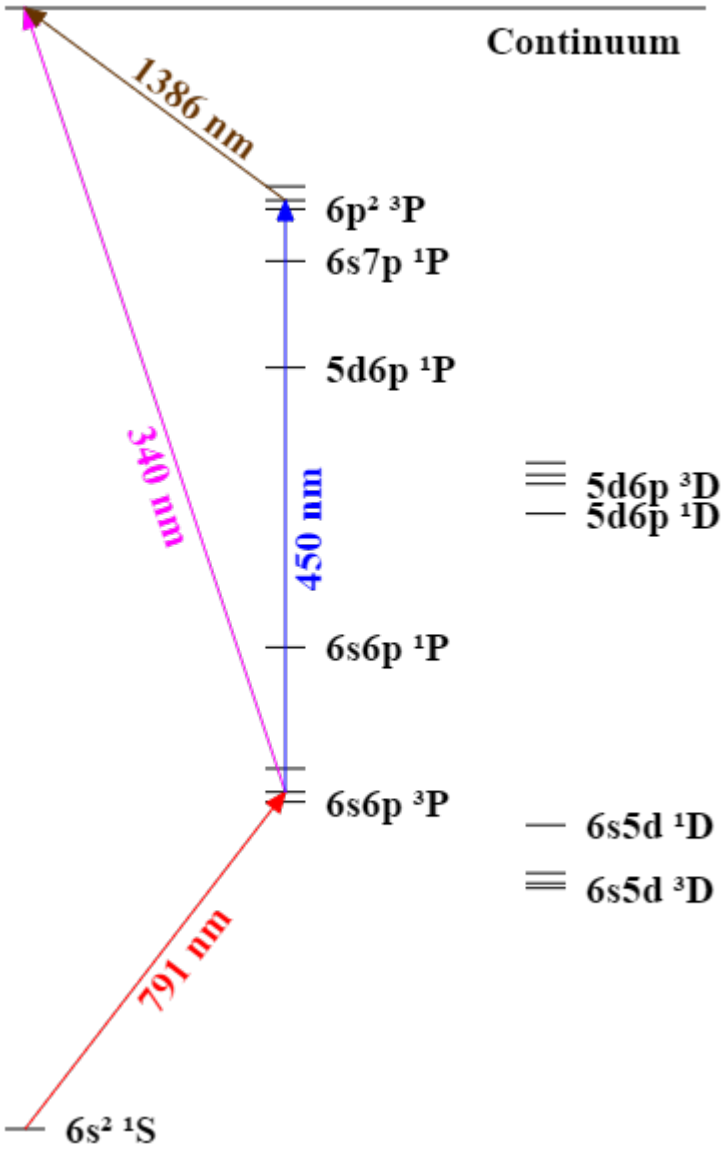

Figure 4.1: Energy levels of neutral barium (to scale) [**?**]. Possible ionization paths including direct, via 6s6p ^{3}P and then direct, and via 6s6p ^{3}P and 6p^2 ^{3}P are shown.

The spectrum of neutral barium provides many different possibilities for ionization schemes as shown in Figure **??**. Originally, we directly ionized with a xenon-mercury arc lamp. This method is not isotope selective and the lamp is generally very difficult to focus. We then switched to use a two laser scheme, first driving a transition from the $6s^2$ ground state to a 6s6p $^3P_1$ excited state and then ionizing using a 337 nm nitrogen laser. The first transition, accomplished using a single mode laser diode at approximately 791 nm, provides isotope selectivity. In addition, both transitions are driven by lasers that can be reasonably focused near the trapping location.

The 791 nm laser is stabilized using a side-of-the-fringe locking circuit to a low finesse optical cavity. This circuit subtracts a constant value from the voltage output of a transimpedance amplifier connected to a photodiode behind the optical cavity. This voltage provides an error signal that when fed back to the piezoelectric element in the ECDL with a PID controller will stabilize the frequency of the laser to a frequency on the side of the cavity line shape. The cavity itself is temperature stabilized with another PID controller feeding back a temperature signal from a thermistor onto the current through a resistive heater using a MOSFET in the linear regime. We observe short term frequency stability of a 1-3 MHz and long term stability of 10-20 MHz most likely due to residual variation in temperature and uncontrolled changes in atmospheric pressure.

This method of ionization has been very successful for a long time. The only downside is that it still uses a fairly energetic beam in the 337 nm nitrogen laser. This laser is energetic enough to easily ionize material deposited on the trap surfaces nearby which can create stray, uncontrolled electric fields that perturb the position of the ion. This ionization becomes increasing problematic for wavelengths below 400 nm [**?**]. In macroscopic Paul traps, this issue has never caused any serious problems because the trap surfaces are several hundred microns from the trapping location and the ionization lasers can be well focused between these surfaces. When working with chip traps, the trapping region is only separated from the nearest surface by 50-80 microns, and this charging can be a more serious issue.

After some initial difficulties trapping in surface traps, we switched to a different ionization scheme that uses only longer wavelength lasers. The initial step is still the transition driven by the 791 nm laser, but then we instead drive a second intermediate transition to

the $6p^2\ ^3P_1$ state using a 450 nm ECDL. From this excited state the 791 nm or any other laser provides sufficient energy to complete the ionization.

Ytterbium is a lanthanoid and has 14 more protons and electrons than barium. These additional electrons are often bound in the 4f subshell and again there is a single valence electron in the 6s subshell that is easy to analyze. There is the additional complication that one of the electrons from the 4f subshell can sometimes be excited to higher energy subshells giving rise to some addtional energy levels with an inner shell vacency. For the most part these levels do not cause any problems, and operations can be as simple as with barium.

Currently we ionize ytterbium using a two-step isotope-selective process. The neutral atom is addressed with a 399 nm laser that drives a transition from the ground state to $4f^{14}\ ^1S\ 6s6p\ ^1P$ singlet state which provides isotope selectivity (see Figure **??**). We then ionize using the same nitrogen pulse laser that can be used to ionize barium. Once we have set up our ytterbium cooling lasers, the 369 nm cooling beam will be a more efficient ionization path from the intermediate state.

When the atoms are ionized they are travelling in a hot thermal beam, and then suddenly they are affected by the trapping fields. The depth of the trap is approximately 3 eV which corresponds to a temperature of ... . Therefore only a small fraction of the thermal flux can actually be trapped at all. Those ions that are confined need to be cooled to a much lower temperature in order to be well localized so that other operations can be performed on them.

4.2 Doppler Cooling

This initial cooling can be accomplished by a technique called laser Doppler cooling. A strong transition in the ion is addressed by a laser detuned to a frequency slightly lower than the center of the transition. Cooling is then accomplished because of the effect of the Doppler shift because of the ions motion. When the ion is moving towards the source of the laser, the ion sees an increased laser frequency which is closer to the center of the resonance. Therefore the ion scatters more flourescence when it is moving towards the laser than when it is moving away from it.

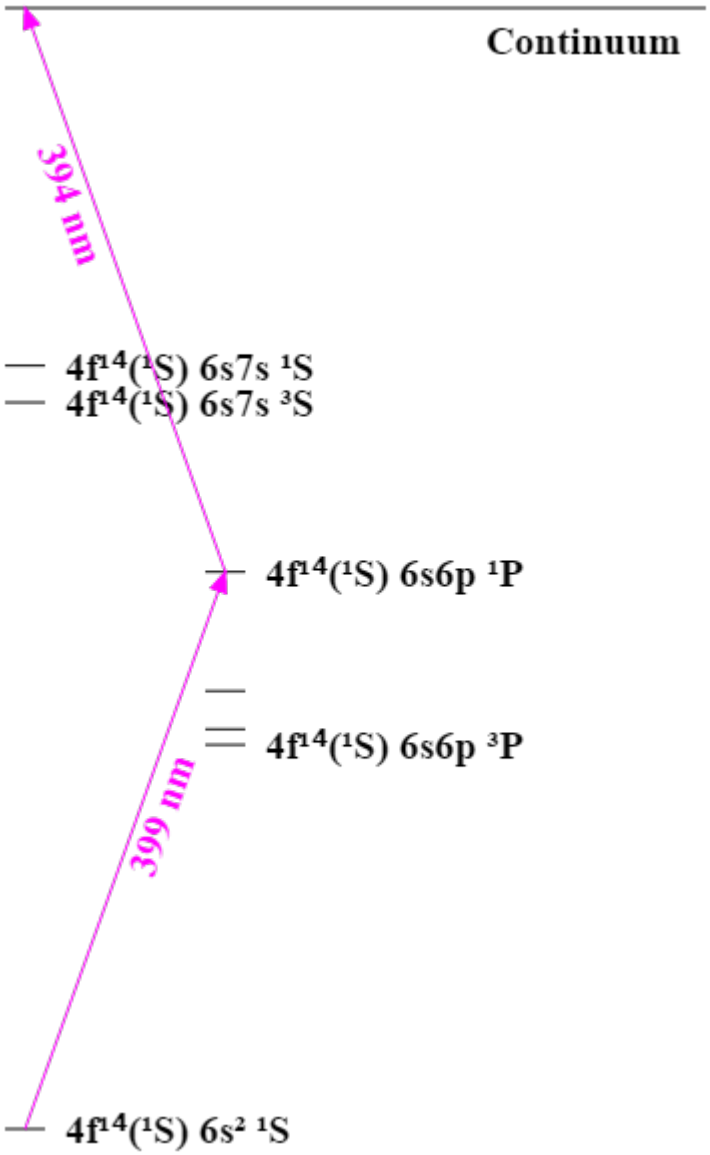

Figure 4.2: Energy levels of neutral ytterbiun (to scale) []. Ionization is achieve using a 399 nm laser beam and a 369 nm laser beam also needed for laser cooling.

The rate at which an ion scatters photons from a source can be found as

$$r_{scatter} = \frac{\Gamma}{2}\frac{s}{1+s+\frac{4\delta^2}{\Gamma^2}} \tag{4.1}$$

where Δ is the linewidth of the atomic transition, s is the saturation parameter, and δ is the frequency detuning between the source and the center of the atomic transition. Each photon scattering event also transfers the momentum from the photon to the ions motion. Therefore the scatter rate can be rewritten as a force on the ion

$$F_{\text{scatter}} = \hbar k r_{\text{scatter}} = \hbar k \frac{\Gamma}{2}\frac{s}{1+s+\frac{4\delta^2}{\Gamma^2}} \tag{4.2}$$

where $k = \frac{\lambda}{2\pi}$ is the photon wavenumber.

The Doppler shift affects this force by causing an additional frequency shift on the detuning. The detuning δ can be rewritten for small ion velocities as $\delta - kv_{ion}$, where v_{ion} is the velocity of the ion with respect to the laser. Cooling can be achived by choosing these parameters such that the ion experience a force of the form $F = -\gamma v_{ion}$ that acts in opposition to its velocity. For small velocities the scatter force has the form

$$\begin{aligned} F_{\text{scatter,doppler}} &\approx F_{\text{scatter}} + kv_{\text{ion}}\frac{\partial F_{\text{scatter}}}{\partial \delta} && (4.3)\\ &= F_{\text{scatter}}\left(1 - \frac{8k\delta/\Gamma^2}{1+s+\frac{4\delta^2}{\Gamma^2}}v_{\text{ion}}\right) && (4.4)\end{aligned}$$

where we can identify the term multiplying $\mathrm{v_{ion}}$ as the damping force coefficient.

The minimum temperature that can be reached by Doppler cooling is set by the random impulses the ion feels when it emits photons that it has absorbed. Although these photons are randomly directed and average to no net contribution to the momentum, the ions temperature is still affected by them. The resulting calculation is easiest to consider from an energy standpoint. Balancing the cooling rate of the lasers and the heating rate from these fluctuations, the minimum energy can be found to be

$$E_i = \hbar\left(1 + \frac{f_{\text{scatter}}}{f_{\text{absorb}}}\right)\frac{(\Gamma/2)^2+\delta^2}{8\delta}, \tag{4.5}$$

where f_{scatter} is the probability for the ion to scatter a photon in the $\hat{x}_i$ direction and f_{absorb} is the component of the Doppler cooling beam parallel to the $\hat{x}_i$ direction.

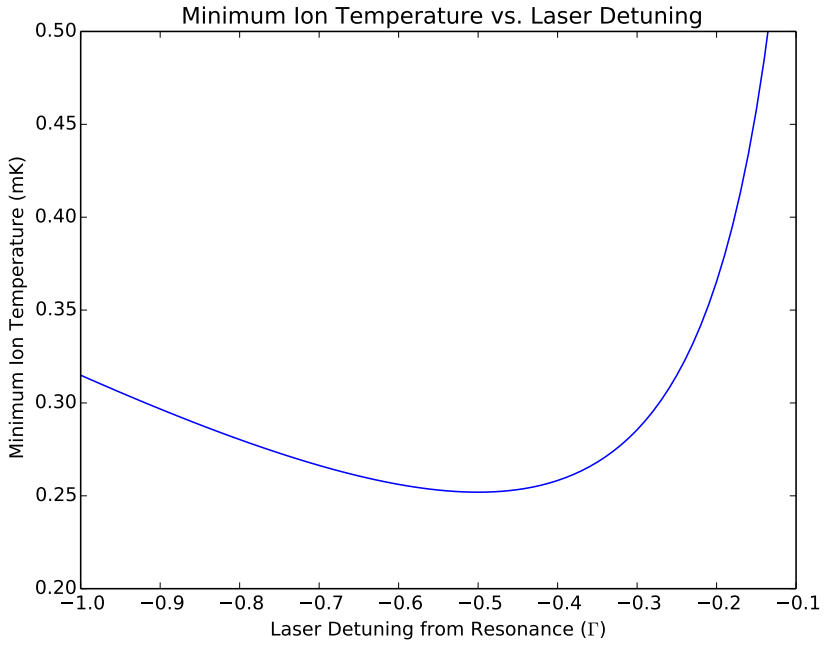

Figure 4.3: Minimum ion temperature for barium ions as a function of detuning of the Doppler cooling laser from resonance in units of the natural linewidth Γ. The temperature reaches a minimum of ≈ 0.25 mK at a detuning of -0.5 * Γ.

Doppler cooling Barium involves using two lasers. The 493 nm transition is chosen to be the transition to actually cool the ion. Unfortunately, there are two possible decay paths from the $6P_{1/2}$ state that the 493 nm laser excites. The ion can decay directly back to the $6S_{1/2}$ ground state from which the 493 nm transition may be driven again to continue cooling, but it may also decay to the long-lived $5D_{3/2}$ state. Since the lifetime of this state is $\approx$ 30 s it is necessary to use a second laser to depopulate this state in order to scatter enough 493 nm photons to cool the ion.

The 650 nm laser is provided by an external cavity laser diode directly providing apprxomiately 7 mW of optical power, but there were no avialable 493 nm diodes at the times the setup was designed. Instead we have a 986 nm ECDL that produces approximately 150 mW of optical power. The 986 nm light is sent through an AOM and the first order diffracted beam is sent through a periodically-poled lithium niobate doubling crystal to produce 493 nm light. Since this switching is performed in the infrared light the isolation is doubled in the blue light sent to the ion, and we have measured isolation of more than 50 dB. The 650 nm light is shuttered using a single or double passed AOM depending on the needs of the experiment being performed.

These lasers are already sufficiently stable on short time scales to perform Doppler cooling, but they both exhibit slow frequency drifts on the order of 1 MHz/min that makes it difficult to perform long experiments without stabilization. For this reason both lasers are stabilized to optical cavities. The light sent to the optical cavities is offset by an adjustable frequency offset using a DPAOM. The frequency detuning of the DPAOM is modulated at 20 kHz to modulate the cavity signal. A phase shifter, frequency mixer, and low pass filter are used to demodulate the cavity signal with the reference 20 kHz modulation signal. The result is an error signal that crosses zero at the top of the cavity signal. The error signal is sent through a PID controller and then to a piezoelectric element controlling the feedback frequency inside the ECDL. As shown in Figure **??**, the light being sent to the optical cavity comes from the 0^{th} order of an AOM used for shuttering the light going to the vacuum chamber. For this reason, the optical power sent to the cavities can vary by a factor or 5 to 10. The circuit described here is insensitive to this change in power because it stabilizes the laser to the top of the fringe, whereas the side-of-the-fringe circuit described

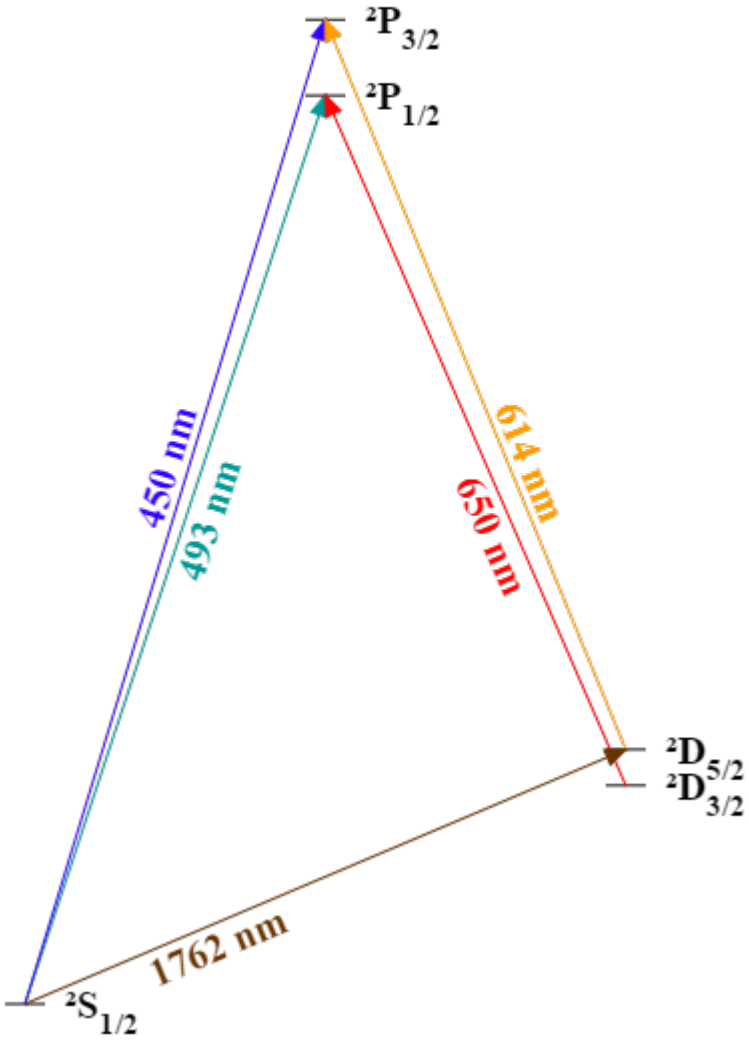

Figure 4.4: Energy levels of singly ionized barium (to scale) [**?**]. Laser cooling is accomplished using the 493 nm transition with a 650 nm repump. The $D_{\frac{5}{2}}$ is used as a "shelving" state that is outside of the cooling cycle.

earlier would cause large frequency shifts whenever the shuttering AOM was switched.

Cooling Ytterbium also involves a repump laser. The cooling transition is at 369 nm and can be reached using a direct diode cooled to a few degrees celsius. The excited state that is reached via this transition can also decay to a long-lived $6D_{3/2}$ state. Unlike in barium, it is most convenient to depopulate this state using a transition to a different excited state formed by exciting an electron from the f shell. This transition at 935 nm does not introduce any other long-lived possible decay states and the cooling cycle is closed. There is one other complication in working with ytterbium though. The ion can be collisionally excited to the $5F_{7/2}$ state, which has a lifetime of 7 years. We currently do not have any way to repump from this state, which will limit the useful lifetimes of the ytterbium we trap.

The Ytterbium lasers are not currently shuttered in any way, although that will be necessary to perform quantum operations on ytterbium ions eventually. They are again stabilized to optical cavities using a side of the fringe locking circuit similar to the one used with the 791 nm laser.

4.3 Initialization and Readout

Now we have successfully ionized, trapped, and cooled both Barium and Ytterbium ions. In order to begin performing quantum information operations on this system, we need to find qubits in both that will satisfy the DiVincezo critera from Subsection **??**. In particular we need to choose two energy states that can be initialized to some simple state representing $|0\rangle$, stay coherent for long enough for our computation to take place, and then be measured.

Ytterbium-171 has some very desirable properties for implementing these criteria. It has nuclear spin $\frac{1}{2}$, which means that its ground state is split into two hyperfine levels with $F = 0$ and $F = 1$. The $F = 0$ hyperfine level has only one possible m quantum number $m_F = 0$, which is obviously not magnetically sensitive. The hyperfine splitting between the two F levels is 12.6 ... GHZ [], and therefore laser line widths are small enough to frequency select which level to address. The $F = 1$ hyperfine manifold has three possible magnetic moment alignments $m_F = -1, 0, 1$, and again there is a magnetically insensitive energy level available. These two magnetically insensitive energy levels make excellent qubit levels. Coherence times of greater than a second have been measured without any kind of

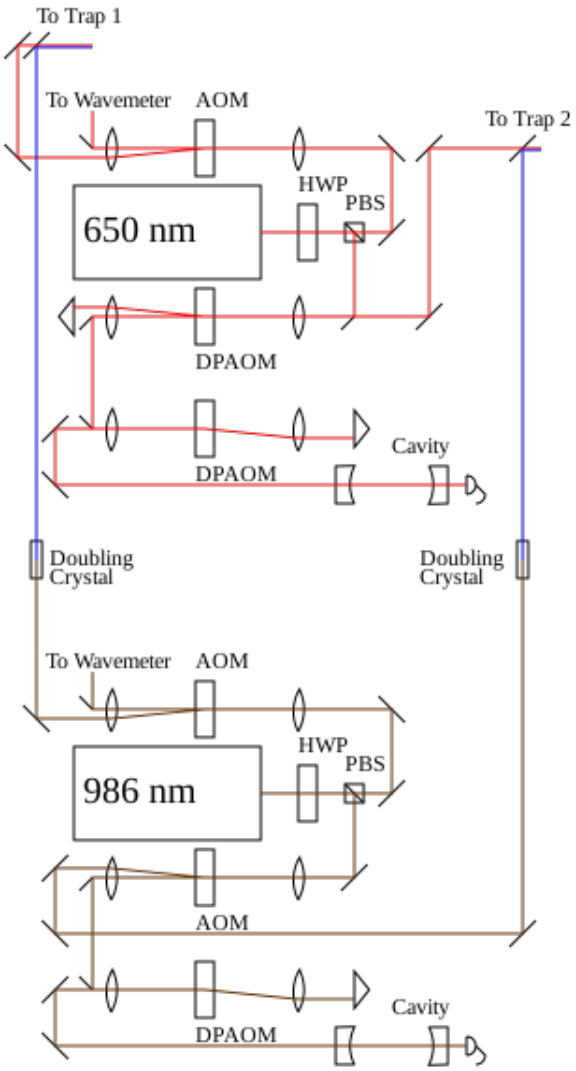

Figure 4.5: Layout of optics for Doppler cooling Barium ions. A 650 nm ECDL and a 986 nm ECDL are both used with the 986 nm laser being doubled to 493 nm light using a PPLN crystal. Both lasers are divided into two separate paths to cool ions in separate vacuum chambers with the amount of power in each beam controllable by a HWP. The lasers for each trap are then combined using a dichroic mirror and sent to the traps via single mode fiber (not shown).

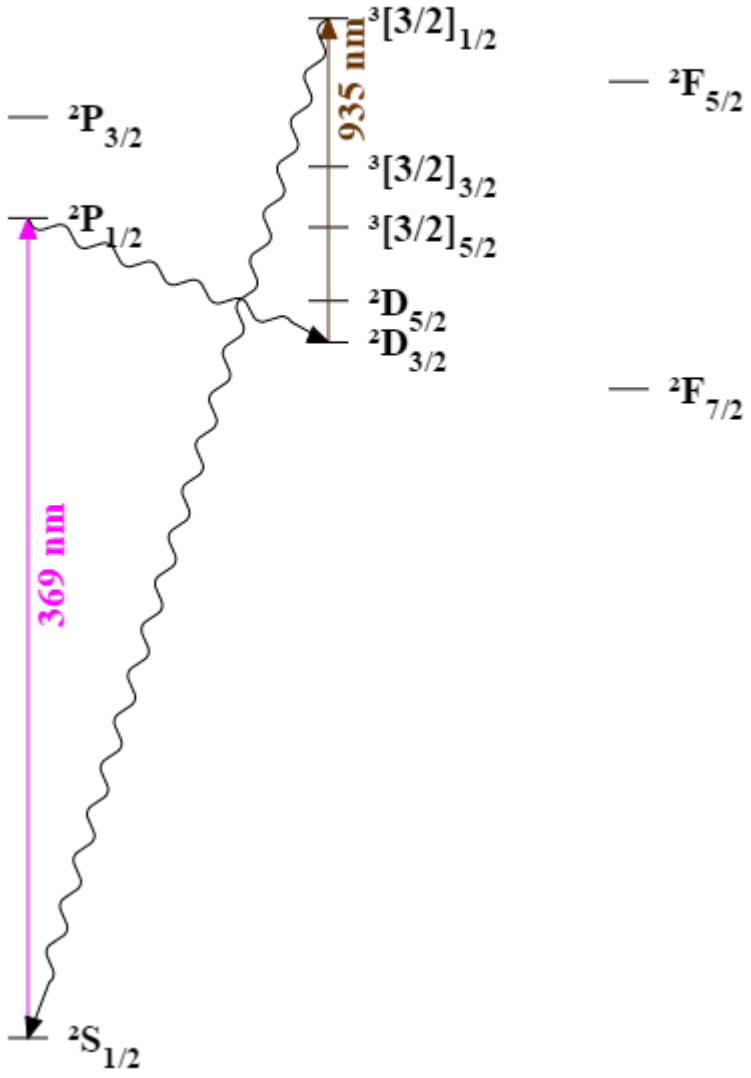

Figure 4.6: Energy levels of singly ionized ytterbium (to scale) []. Laser cooling is accomplished using the 369 nm transition with a 650 nm repump.

magnetic shielding [].

Initialization and readout of these energy levels is also very easy. In order to address both levels, a 1 MHz linewidth laser can be tuned to the energy difference between the $F = 1$ manifold in the $S_{\frac{1}{2}}$ ground state and the $F = 0$ manifold in the $P_{\frac{1}{2}}$ excited state. Due to angular momentum conservation the decay to the $F = 0$ manifold of the ground state is forbidden. The ion will therefore continuously absorb and emit light on this transition until it off-resonantly scatters to the $F = 1$ manifold in the excited state.

Ytterbium-174 has none of these beneficial properties, but it is more naturally abundant and easier to cool because there are no additional hyperfine levels that need to be addressed to close the cooling cycle. For this reason, and other experimental limitations we are currently working with Yb-174 instead, but actual quantum computation experiments will use Yb-171 in the future.

Choosing a qubit for operations in barium is somewhat more complicated. There are three possible isotopes that might be considered for use in quantum computation. Barium-138 is most naturally abundant isotope and it has nuclear spin 0, and therefore there is no hyperfine structure to complicate its energy diagram. Barium-137 has hyperfine structure because of its nuclear spin with I=$\frac{3}{2}$, however this does not give rise to the same nice properties as with I=$\frac{1}{2}$. There are many more long lived states that have to be repumped and no simple selection rules allowing for easy detection. There is an isotope of barium, Barium-133, with nuclear spin I=$i\frac{1}{2}$, but it undergoes radioactive decay with a half-life of 10.51(5) yrs []. Therefore an enriched sample must be used in order to work with this isotope.

Instead we have been working with the most abundant natural isotope, Barium-138. $^{138}Ba^{+}$has no nuclear spin and therefore no hyperfine structure. Its ground states is a $6S_{\frac{1}{2}}$ level with two Zeeman sublevels $m_J = \pm\frac{1}{2}$. These levels are very sensitive to magnetic field and maintaining coherence beyond a significant fraction of the ac wall period would be difficult. Fortunately, following the description of our architecture given earlier we don't need to store quantum information in both species for long periods of time. Barium ions can be used to cool the ytterbium ions and to generate remote ion entanglement events. The remote entanglement generate between barium ions can easily be transferred to ytterbium

ions using a gate sequence of a few hundred microseconds. Since we can work around these problems and the ground state Zeeman levels are otherwise relatively easy to work with, we have chosen them to be the qubit levels in our current architecture.

Initialization of these levels is again fairly straightforward. Circularly polarized light can be utilized in a technique called optical pumping to initialze the ion into either Zeeman state. Again because of conservation of angular momentum the two circular polarization of light along the ions quantization axis $\sigma\pm$ must correspond to transitions with $\Delta m_J = \pm 1$. Since the 493 nm transition in ionized barium transfers population between two states with angular momentum $J = \frac{1}{2}$, σ^+ 493 nm light cannot drive a transition from $6S_{\frac{1}{2}} m_J = +\frac{1}{2}$ to any other state. However, this light can drive transitions between the $m_J = -\frac{1}{2}$ level and the $6P_{\frac{1}{2}}$ state. Once the transition is driven, the polarization of the emitted light and therefore the resulting ground state Zeeman level is random. However, after the σ^+ polarized 493 nm light has been applied for a long period of time population will accumulate in the $m_J = +\frac{1}{2}$ level because no lasers are addressing this level.

In other trapping systems we have implemented this procedure using two separate 493 nm beams. One beam is focused onto the ion with linear polarization with respect to the ions quantization axis and therefore can drive either transition and will Doppler cool the ion. The other beam is sent in with a circular polarization, which will initialize the ions state to the dark ground state level but not cool effectively. By shuttering the linearly polarized beam, the ion can be optically pumped to the state the circularly polarized beam does not address.

Since our setup switches the 986 nm beam before it is frequency doubled the optical pumping procedure can not be implemented in the same way because we cannot independently shutter two 493 nm beams well. Instead a single 493 nm beam is sent to the trap. The beam passes through a quater wave plate which initializes it to a circular polarization and then through a Pockels cell. The Pockel's cell is oriented so that when charged to 1.1 kV the 493 nm beam can be rotated back towards linear polarization. Therefore the 493 nm beam can be switched from performing Doppler cooling to performing optical pumping as quickly as the voltage can be switched in the Pockels cell. We use a modified piezeoelectric actuator driver circuit to implement this switching in 2 ms or less based on a TTL signal.

In the final quantum computing device there will be no need to read out the state of the barium ions, and the short coherence time of the Zeeman sublevels will not present a significant challenge. However, at the moment we have not completed setting up the infrastructure to allow us to transfer quantum entanglement to the ytterbium ion or the equipment to readout the state of the ytterbium ions. Instead we are currently performing experiments with only the capability to control and measure the quantum state of the barium ions.

In order to readout the Zeeman levels of the barium ions we cannot play a simple trick as in ytterbium. Unfortunately there are no selection rules to protect decays from the excited state to either of our qubit states. Instead we have to transfer the population from one of the qubit states to a long-lived state outside of the cooling cycle. In Figure **??**, we can see that there is such a state, the $5D_{\frac{5}{2}}$ state. The $5D_{\frac{5}{2}}$ state has a lifetime of 30 s [], which is more than sufficient since we can determine whether the ion is in the cooling cycle by monitoring its flourescence for 20 ms or less.

Population can be transferred to the $^{138}Ba^{+}5D_{\frac{5}{2}}$ using a narrow, 1762 nm fiber laser. This laser produces $\approx 10\ mW$ of optical power with a linewidth of $\approx 100\ Hz$ []. It is locked to a temperature and pressure stabilized, Zeroder optical cavity with a linewidth of 500 kHz []. With the power left after frequency stabilization, coherent pi-pulses from the $6S_{\frac{1}{2}}$ ground state to the $5D_{\frac{5}{2}}$ excited state can be achieved in 10 us. Since the natural linewidth of the transition and the Rabi frequency with which we drive it are both much smaller than the separation between the two Zeeman levels we can frequency select which Zeeman level we are addressing.

Using this laser readout of the Zeeman state of the $^{138}Ba^{+}$ion is achieved by transferring of "shelving" one of the Zeeman states to the $5D_{\frac{5}{2}}$ level. The cooling lasers are then applied for 20 ms and a simple threshold is again used to separate background PMT count from the counts of a flourescing ion. The ion will only be flourescing if the valence electron was initially in the unshelved Zeeman state. Once this determination has been made, if the electron was successfully shelved it can be brought back into the cooling cycle without having to wait for the $\approx 30\ s$ coherence time by applying light at 614 nm (see Figure **??**).

Part III

MEASUREMENTS OF SURFACE TRAPS AND MIXED SPECIES ION CHAINS

Chapter 5

SURFACE TRAPS

Surface electrode traps have several advantages over standard "macro" ion traps. They can be repeatably manufactured and provide large number of independent dc voltage parameters that can be used to precisely control ions' location and motion. We have performed some initial characterization of surface traps that we have been working with.

5.1 Ion Dark Lifetime

One of the initial difficulties with working with surface traps was their poor ion lifetimes. Even while being cooled ions would only stay trapped for minutes, and without continuous cooling lifetimes were often as small as a few seconds. The first trap that we performed measurements in was a Sandia National Labs "Y" trap. This surface electrode trap has three arms extending radially from a central point where they are all connected. The radial trap is formed by rf and dc rails that run along the side of each arm. Near the end of each arm there is a 100 micron by 100 micron hole through the entire chip that allows neutral atom flux to travel from behind the trap to be loaded into the trapping region above it.

Cooled lifetimes in this trap were easily tens of minutes, and further investigation of them would have painfully slow so we performed measurements of the dark, uncooled lifetime instead. An automated loading procedure was developed leveraging the completely autmoatic control over all ionization lasers and our neutral atom oven. This system allowed the entire experiment to be automated even though it involved losing and retrapping ions many times.

Measuring dark lifetimes itself is straightforward. A single ion is trapped and cooled using our normal cooling apparatus. The cooling lasers are then well shuttered for a fixed period of time. The cooling lasers are unshuttered and flourescence is collected to determine if the ion remained in the trap. If it didn't another ion is trapped, and then the experiment

is repeated.

This measurement is expected to give some insight into the heating rate of ions in the trap. The heating rate of ions traps is complicated but is related to the stray field and electric field noise environments of the ion. Using our shuttling system we were able to repeat the measurement at different location along one arm of the trap. It was expected that because of the neutral atom flux deposited underneath the loading hole this region could develop a large stray vertical field which would increase heating in this region.

Motional heating in ion traps is a complicated phenomenon and is only recently beginning to be investigated systematically. There are a number of phenomena known to cause some heating including rf electric field noise near trap junctions, DAC sampling noise, and electric field noise at the secular frequencies [**?**, **?**]. The first heating source is significant in junctions in surface traps where there may be significant gradients in the rf pseudopotential. In regions with high gradients, the ion can provide nonlinear mixing between applied rf and the applied trapping rf to excite motional energy in the ions. The update rate of the DACs has strong frequency components that can cause direct heating of motional modes or combinations of motional modes through parametric resonances.

Direct heating from electric field noise at the motional secular frequencies has historically been anomalously high. Heating rates seem to strongly increase as ions are brought closer to surfaces in ion traps, which has made the problem increasingly problematic as the community moves towards using surface traps where ions are located 40 um to 100 um from the surface of the trap. The expected scaling for the heating rate as a function of the distance to the nearest surface would be d^{-2}, but instead there is significant evidence that the dependence is d^{-4}. This problem has often been addressed in the past by using cryogenic instead of room temperature ion trap systems which greatly reduces the electric field noise density [**?**, **?**, **?**]. Recent investigations have shown that this surface heating is probably due to electric field noise in contaminants deposited on the surface during the UHV bakeout [**?**, **?**]. These contaminants can be removed by argon ion bombardment after bakeout, which significantly lowers the heating rate in the trap.

While we begin to develop an understanding of the processes behind this heating rate, at the moment it is still one of the most difficult experimental problems in surface traps. In

trapping systems that were not designed to be cleaned by ion bombardment, characterizing and dealing with the trap heating rate is important.

From Figure **??**, it is clear from our results that there are additional heating sources near the loading region. It is beneficial to have regions of the surface trap that do not have loading holes where the heating rates may be lower and quantum operations can be performed more easily. An additional benefit is that ions can be loaded while quantum operations are being performed without the neutral atom flux perturbing the calculation. Even in the loading hole we observe ion lifetimes easily sufficient for quantum operations.

5.2 Secular Frequencies and Stray Fields

As discussed in Section **??** the ions' restoring force from the rf fields is called its secular frequency. Measuring the secular frequencies allows us to characterize the strength of the trapping potential. A common technique to measure these frequencies is to apply a small amplitude electric field and scan its frequency over the possible range for the ions secular frequency. When this "tickle" frequency is resonant with the trap secular frequency the ion is heated [**?**, **?**]. The motion of ions in a Paul trap is given by Equation **??** if there is no stray electric field at the trapping location. Additional micromotion caused by a stray field, $\vec{E}$, adds a term $B_x = q\vec{E} \cdot \hat{x}/m\omega_x^2$. The motion of the ions is described by

$$x(t) = (B_x + A_x \cos(\omega_x t + \phi_x)) \left(1 + \frac{q_x}{2} \cos(\Omega t)\right), \tag{5.1}$$

where ω_x is the secular frequency, Ω is the frequency of the applied rf, q_x is a parameter of the Mathieu equation, and A_x is an amplitude set by initial conditions. Modulating the applied rf at a frequency ω_m, changes the equation of motion for the ion to

$$\ddot{x} + \omega_x^2 \left(1 + 2m \cos(\omega_m t)\right) x = 0 \tag{5.2}$$

where m is the modulation depth of the applied signal. The system is a driven harmonic oscillator, which will exhibit very largy amplitude driven motion when ω_m is near ω_x.

The additional motion caused by large "tickle" amplitudes can be detected by observing the ion flourescence on a CCD camera where the amplitude of the ions motion can increase to resolvable distance scales. Since the motion of the ion is much faster than the exposure

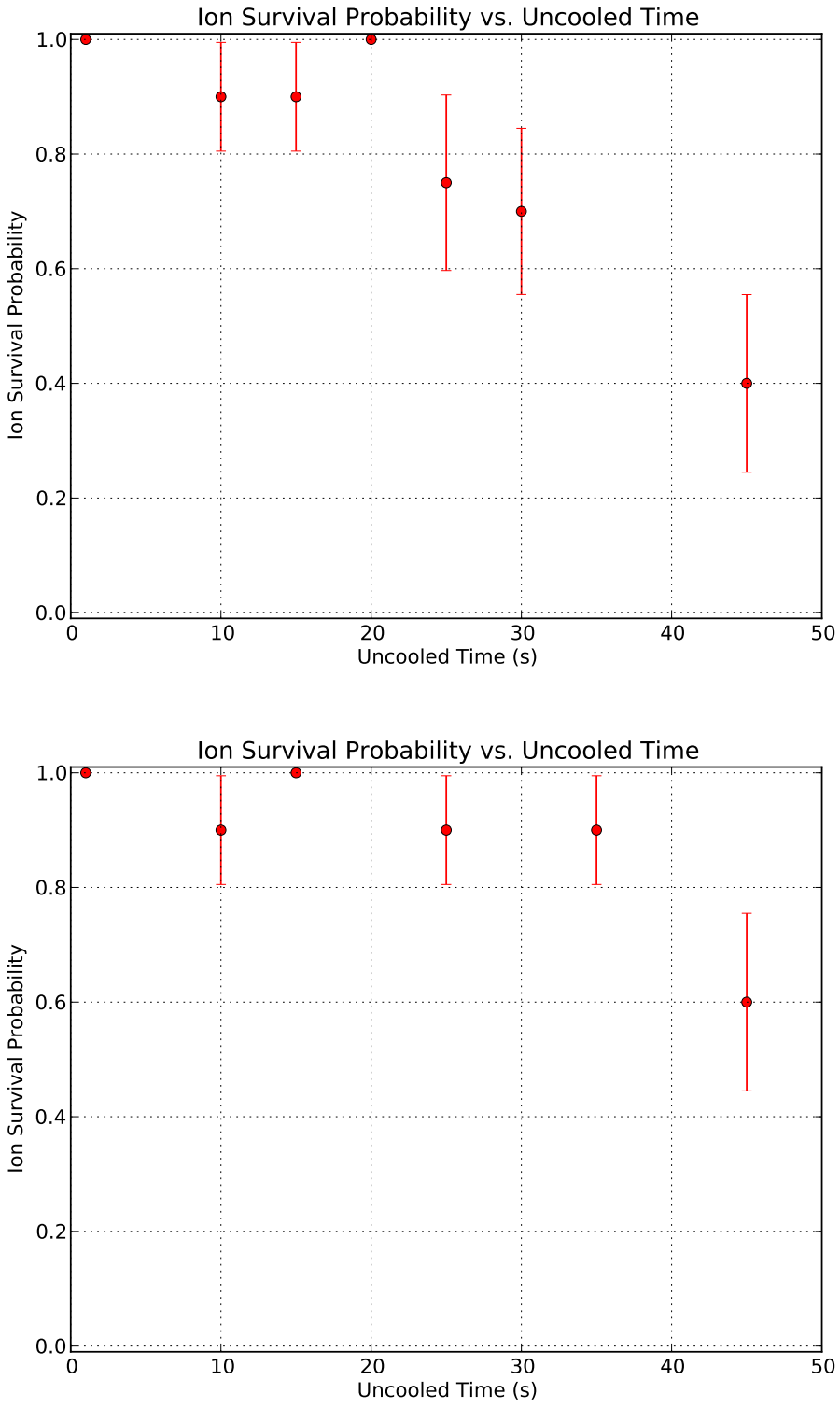

Figure 5.1: The probability that an ion remains trapped and can be recooled after a period without Doppler cooling. This lifetime is significantly shorter in the loading hole (left) than several hundred microns away (right).

time of the camera, the ions' flourescence appears to blur out over a larger area while it is being heated and collapse to a small point when cold. The direction of this blurring can be seen in the CCD images and used to identify the trap axis that is being excited. Figure **??** shows the ions response to being driven at its axial secular frequency. For small amplitudes, the additional heating can be detected by detuning the Doppler cooling laser several linewidths from the transition so that normally the flourescence is very low. When the ion is heated though it occupies much higher motional states and additional flouresence can be seen.

Another method for applying the "tickle" amplitude is to apply an additional frequency to the rf electrodes inside the trap. When this signal's frequency is offset from the rf trap frequency by one of the traps secular frequencies heating can again be observed. The tickle signal is added to the normal trapping rf using an rf splitter/combiner before it is amplified. Although the rf then passes through a resonator with a Q factor of ≈ 200, enough of the probe signal remains for the additional heating to be detected.

The advantage of applying the signal this way is that the amplitude of the heating signal the ion sees is minimized when the ion is located on the rf null. At the rf null the ions micromotion is minimized and therefore the strength of the secular frequency signal that the ion experience is also minimized. By applying the rf in this manner and minimizing the ions response to it the micromotion in all three axes can be minimized.

Using this measurement technique we have measured the secular frequencies of our trap with the voltages we are currently applying. The axial frequency is ≈ 0.75 MHz and the radial frequencies are ≈ 1.50 MHz and 2.05 MHz. In future traps we will extend this to minimize stray fields.

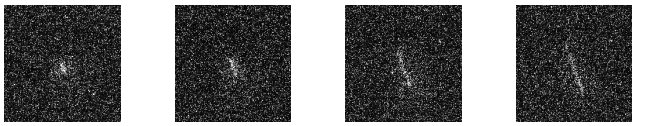

24.171 MHz 24.173 MHz 24.176 MHz 24.178 MHz

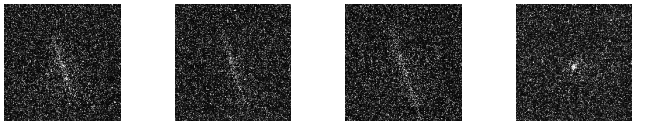

24.181 MHz 24.183 MHz 24.185 MHz 24.187 MHz

Figure 5.2: CCD images of ion flourescence at different applied rf tickle frequency. The amplitude of the ions motion increases dramatically when the tickle frequency is offset from the carrier frequency by the trap's secular frequency.

Chapter 6

MIXED SPECIES NORMAL MODES

The motional states of trapped ions are shared between all ions in the trap and provide a mechanism for transferring information between these ions. By performing sequences of pulses exciting modes shared by two ions, entangling gates can be implemented. In order for this to work the modes must be kept relatively cold using Doppler cooling or other techniques. For chains that include mixed ion species, the normal modes can separate with some modes coupling to one ion species and some to the other. This effect limits our ability to cool both ion species using only cooling lasers addressing one species. We have begun making careful investigation of our ion temperatures and heating rates in mixes species chains. For the moment, we are performing these measurements in a standard macroscopic Paul trap, but we plan to begin using them to characterize different surface trap designs.

6.1 Single Ion Normal Modes

In the case of a single ion occupying a trapping region there are only three normal modes corresponding to the trap strength in each direction. At the bottom of the trap the trapping potentials are harmonic and the motional states of the ion are well described by simple quantum harmonic oscillator states. That is to say that we can label the motional states by $|0\rangle$, $|1\rangle$, etc. with energy $E_n = \hbar\omega(n + \frac{1}{2})$. We can also define raising and lowering operators a and $a^\dagger$ and write the position of the ion in terms of them as $z = z_0(a + a^\dagger)$ where $z_0 = \sqrt{\frac{\hbar}{2m\omega_z}}$ and m is the mass of the ion. After normal Doppler cooling the ion occupies is in a thermal mixed state of these motional levels. The state of the ion is therefore described by a parameter $\bar{n}$, the average motional occupation number and can be described by the density matrix

$$\rho = \sum_{n=0}^{\infty} \frac{1}{\bar{n}+1} \left(\frac{\bar{n}}{\bar{n}+1}\right)^n |n\rangle \langle n| . \tag{6.1}$$

In order to analyze how entangling gates can use these levels we will first make some

simple measurements using them with a single ion. In particular, measurements of $\bar{n}$ and its time derivative $\dot{\bar{n}}$ provide information that is likely to scale to larger numbers of ions in the same trap. The average motional occupation number $\bar{n}$ provides information on how effective Doppler cooling is, and can be indicative of problems with this procedure. The parameters $\dot{\bar{n}}$ is often called the heating rate, and is likely to be roughly constant per ion as more ions are added. Heating rates in macroscopic traps are often less problematic than in surface traps because of the increased distance between the nearest surfaces and the trapping locations.

In order to analyze the normal modes of the ion trap, we have to understand the way electric fields can interact with them. In particular, we will be driving sideband transitions using lasers addressing narrow transitions. In order to gain some understanding of these processes, we will consider a two level atomic system consisting of $|\downarrow\rangle$ and $|\uparrow\rangle$. In addition to these internal energy levels, we will consider motional energy levels in one dimension described by simple harmonic energy levels with energy spacing ω_z. Our base Hamiltonian is therefore

$$H = \hbar\omega_\downarrow |\downarrow\rangle\langle\downarrow| + \hbar\omega_\uparrow |\uparrow\rangle\langle\uparrow| + \sum_{n=0}^{\infty} \hbar\omega_z a^\dagger a \tag{6.2}$$

We will consider the interaction of this Hamiltonian with monochromatic radiation with the Hamiltonian

$$H_I(t) = \hbar\Omega \left(|\uparrow\rangle\langle\downarrow| + |\downarrow\rangle\langle\uparrow|\right)\left(e^{ik_z z + i\omega t + i\phi} + h.c.\right), \tag{6.3}$$

where k_z is the wavevector and ω is the angular frequency of the radiation. Ω is defined as in Chapter **??** to be proportional to the dot product of the electric field magnitude and polarization with the ion dipole moment, $\vec{\mu}\cdot\vec{E}/\hbar$. Transforming this Hamiltonian into the interaction picture, we find

$$H_I(t) = \hbar\Omega\left(|\uparrow\rangle\langle\downarrow| \exp\left(i\eta(ae^{-i\omega_z t} + a^\dagger e^{i\omega_z t}) + i(\omega - \omega_\uparrow + \omega\downarrow)t + i\phi\right) + h.c.\right), \tag{6.4}$$

where $\eta = z_0 k_z$ is the Lamb-Dicke parameter. The effect of the motional modes on the optical transitions can be absorbed into Ω by writing

$$\Omega_{n,n'} = \Omega\left|\langle n'| exp\left(i\eta(a + a^\dagger)\right)|n\rangle\right| \tag{6.5}$$

$$= \Omega e^{-\eta^2/2}\left(\frac{n_<!}{n_>!}\right)^{1/2} \eta^{|n-n'|} L_{n_<}^{|n-n'|}(\eta^2) \tag{6.6}$$

using the generalized Laguerre polynomials L_n^α and defining the smaller of n and n' to be $n_<$ and the larger to be $n_>$. The transition between $|\uparrow\rangle$ and $|\downarrow\rangle$ procedes as in Chapter 1, but with these additional motional degrees of freedom.

Therefore, we can see that we can drive transitions between motional states of the ion. In order to observe these sideband transitions in trapped barium ions we will use the technologies discussed in Section **??**. We will trap and Doppler cool a single $^{138}Ba^+$ion, and then initialize its state to the m_J = -1/2 level of its $6S_{1/2}$ ground state by switching our cooling laser to have circular polarization. We will then shutter the cooling lasers and apply a fixed duration pulse of 1762 nm light that is near the transition from the ground state to the m_J = -1/2 level of the $5D_{5/2}$ state. Upon reactivating the cooling lasers we will see flourescence from the ion only if we were unsuccessful in driving a transition with 1762 nm laser. This procedure is repeated multiple times to build statistics and then repeated at multiple frequencies to explore the frequency dependence of the transition.

Figure **??** shows the result of this procedure. The large center peak is the direct resonance that does not include any change in motional state. There are both red and blue sidebands of this transition visible. The strength of the sidebands is related to the carrier transition by $\sqrt{\eta}\bar{n}$ and therefore depends on the photon momentum, the motional secular frequency, and the occupation number. The two sidebands that are shown are the radial sidebands with secular frequencies of 1.31 MHz and 1.21 MHz. The 1762 nm laser is oriented perpendicular to the axial trap axis and therefore the photon momentum in that direction is zero and no sideband transition can be seen.

Using this technology we would then like to estimate the initial temperature and heating rate of our ions. There are two possible methods for performing this procedure. We could compare the strength of the sidebands to the strength of the carrier and use the weak excitation limit to extract $\sqrt{\eta}\bar{n}$ for each peak. The difficulty with this strategy is that the radial modes must be weakly excited in order to extract this information, and errors on fitting the heights of the peaks are often large. Instead for single ions it is easier to measure the decay of Rabi oscillations.

Since our 1762 nm source has a linewidth $\leq$ 1 kHz we should be able to apply pulses of hundreds of microseconds of duration without seeing any noticable decoherence of Rabi

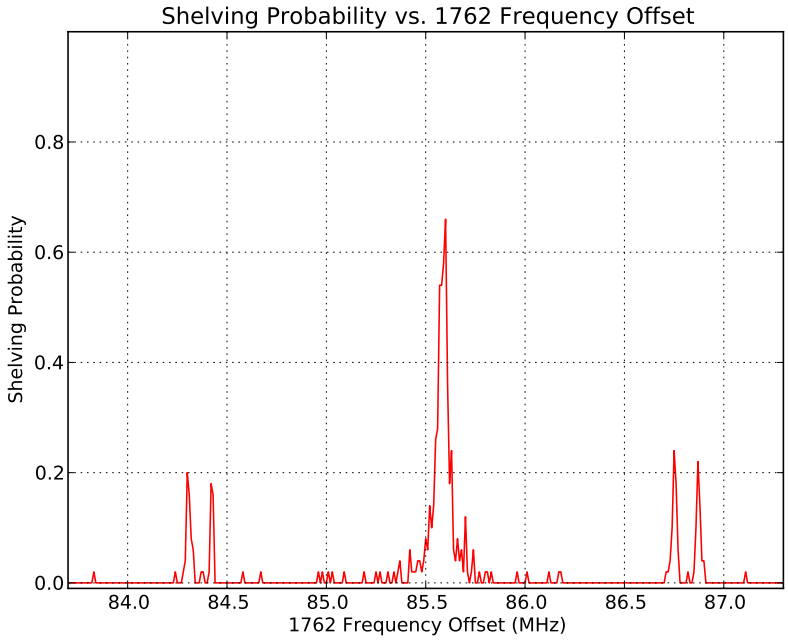

Figure 6.1: Shelving probability as a function of 1762 nm laser detuning. A strong carrier transition is present at offset 85.6 MHz, while symmetric sidebands can be seen at 84.3 MHz, 84.4 MHz, 86.75 MHz, and 86.85 MHz.

oscillations. Instead these oscillations tends to decay in 100 us to 200 us because of the finite temperature of our ions. The source of this decoherence is driving carrier (not sideband) transitions that start in different motional hamronic oscillator states. The sideband transitions are far enough away in frequency that they are not relevant, but these carrier transitions at different motional energies are slightly shifted in frequency with respect to one another. Since the ion is in a thermal state, all of these transitions of slightly different frequency are driven and their interference appears as the decoherence of the oscillations.

The Rabi frequency for these excited motional level carrier transitions follows from the above discussion of sideband transitions and is

$$\Omega_{n,n} = \Omega e^{-\eta^2/2} L_n^0(\eta^2) \tag{6.7}$$

which can be simplified for small η^2 to $\Omega(1-\eta^2 n)$. In order to understand the effect of temperature we can write the probability of shelving as a sum over a thermal distribution of motional states. The shelving probability becomes

$$P_{\text{shelve}}(t) = \frac{1}{2} - \frac{1}{2}\sum_{n=0}^{\infty} \frac{1}{\bar{n}+1} * \left(\frac{\bar{n}}{\bar{n}+1}\right)^n \cos\left(2 * \Omega_{n,n} * t\right) \tag{6.8}$$

This analysis has all been performed assuming there is only one motional degree of freedom. If the ion has multiple modes of motion there is a corresponding Lamb-Dicke parameter, η and thermal average occupation number, $\bar{n}$, for each mode. In order to generate the shelving probability we would have to sum over all possible combinations of occupation number weighted by their thermal probability for each mode. For even a few modes this calculation becomes very time consuming, and it is not possible to easily fit data to the free parameters. Fitting could be done by Monte Carlo sampling from the distribution of occupation numbers, but the fitting time is still large to achieve reasonable accuracy.

Instead we have chosen to only address the radial modes of motion which are separated in frequency by $\leq 10\%$. It is therefore resonable to approximate their occupation numbers and Lamb-Dicke parameters as equal. Since the axial secular frequency is much lower this procedure would not be possible if the 1762 nm laser also addressed this state, but that is not the case. Making this approximation we can extract a parameter $\sum_i \bar{n}_i$, where the

sum extends over the average thermal occupation numbers of the radial modes, from an experimental Rabi flop curve.

Using this procedure, we would like to find the final temperature we achieve with Doppler cooling, as well as the rate at which the ion heats while Doppler cooling is diabled. In order to find this heating rate of the ion, we can allow it to sit uncooled for a period of time before applying 1762 nm pulses to it. In Figure **??** we can see that as we wait longer the ion increases in temperature and the Rabi oscillation decay more rapidly as expected.

Although heating in ion traps is complicated and several heating mechanisms are certainly nonlinear, it is common to approximate it as linear. This approximation holds well at least for small temperatures. As the ion increases in temperature and experiences more of the trap anharmonicity and rf-induced micromotion heating rates tend to increase. The total radial quanta of our single trapped barium ion is fit to 122 quanta, with a heating rate of 2.43 quanta/ms (see Figure **??**.

Unfortunately, the initial temperature of the ion was significantly hotter than would be expected. Doppler cooling barium ions with 493 nm light should result in ion temperatures of . Instead we see Doppler temperature approximately an order of magnitude higher at $\approx$ 50 quanta per radial mode of motion. By modeling the strength of the sidebands we can drive as described above we can tell that our Doppler temperature is not actually this high. Instead, this effect is being caused by frequency variations in our 1762 nm laser.

This laser is locked to a 500 kHz linewidth cavity by a locking circuit that stabilizes it to within a few percent of the maximum cavity signal. This small oscillation still corresponds to a frequency modulation of the laser with a modulation depth of 10 kHz to 20 kHz. This oscillation is very slow compared to timescale of the pulses we apply to the ion. The result is that every run of our Rabi flop experiment sees an approximately constant frequency drawn from this 20 kHz wide distribution of frequencies. The result of this procedure is easily simulated by performing this sampling in software. The shelving probability, P_{shelved}, is given by

$$P_{\text{shelved}}(t) = \int_f \frac{1}{\sigma_f\sqrt{2\pi}} e^{-\frac{(f-\mu_f)^2}{2\sigma_f^2}} \frac{\Omega_{\text{rabi}}^2}{\Omega_{\text{rabi}}^2 + (\omega - \omega_{\text{transition}})^2} * \sin^2\left(\frac{\Omega_{\text{rabi}}^2}{\Omega_{\text{rabi}}^2 + (\omega - \omega_{\text{transition}})^2}\frac{t}{2}\right) \tag{6.9}$$

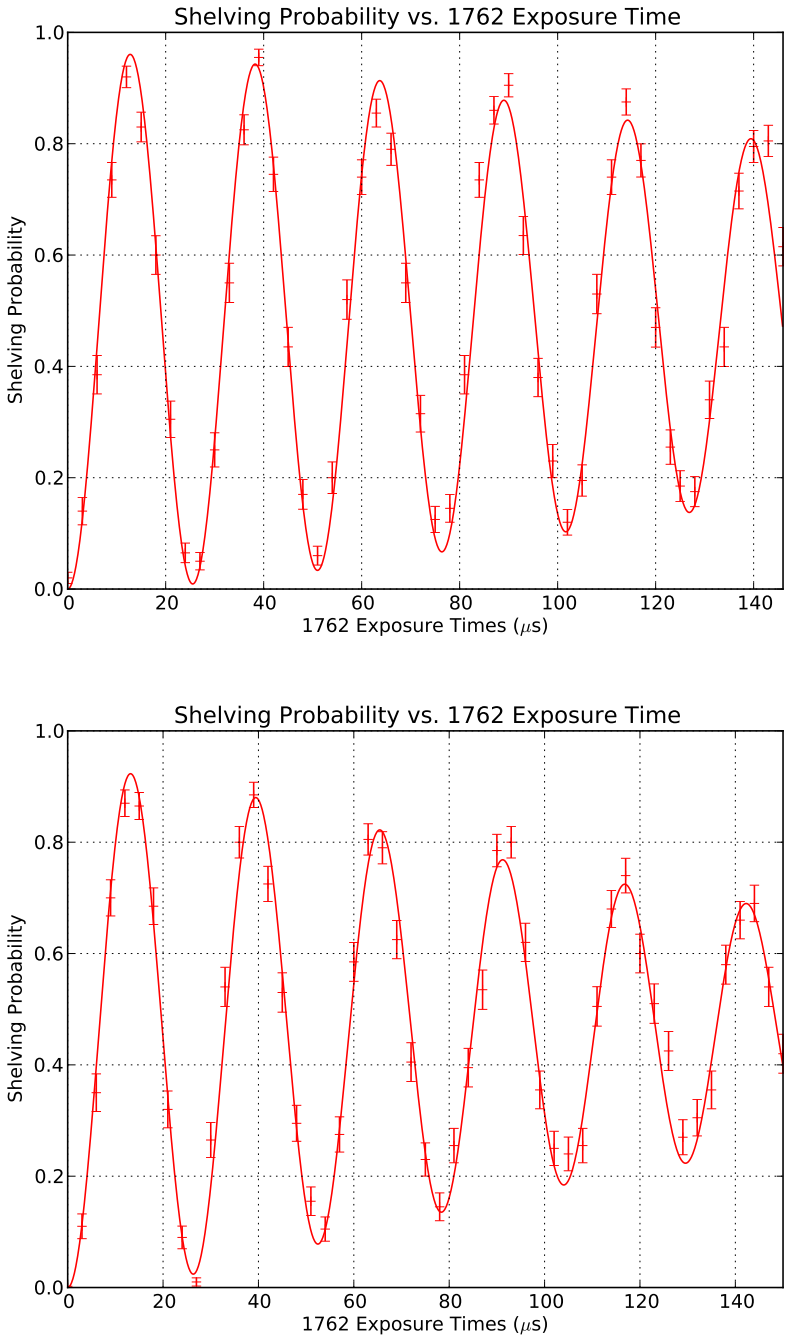

Figure 6.2: Rabi oscillations with different delays between the end of Doppler cooling and the beginning of 1762 nm laser exposure. The Rabi oscillations decay much quicker after a delay of 50 ms (right) than with no delay (left).

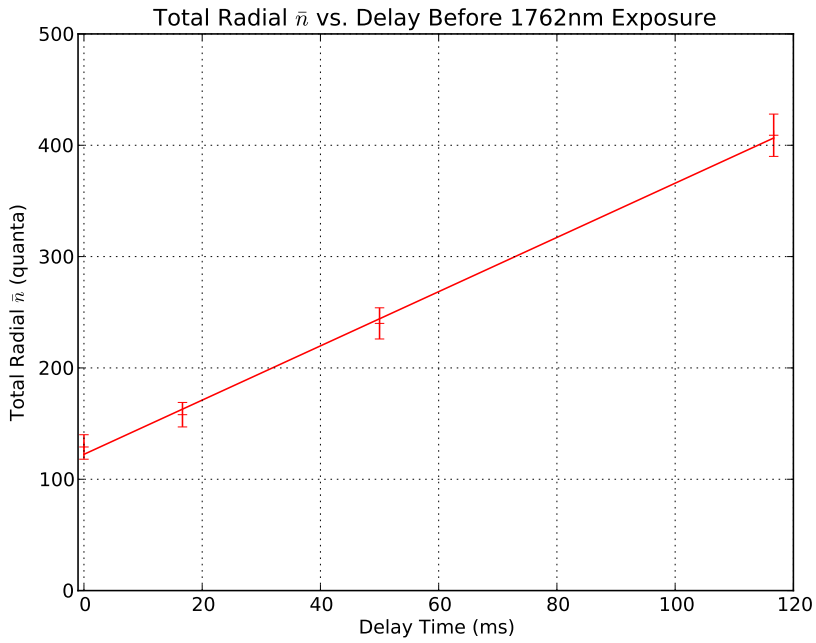

Figure 6.3: Total ion radial quanta is plotted as a function of delay time before the experimental sequence begins during which the ion is not cooled. A linear fit is shown with initial radial average thermal occupation number 122 quanta and a 2.43 quanta/ms heating rate.

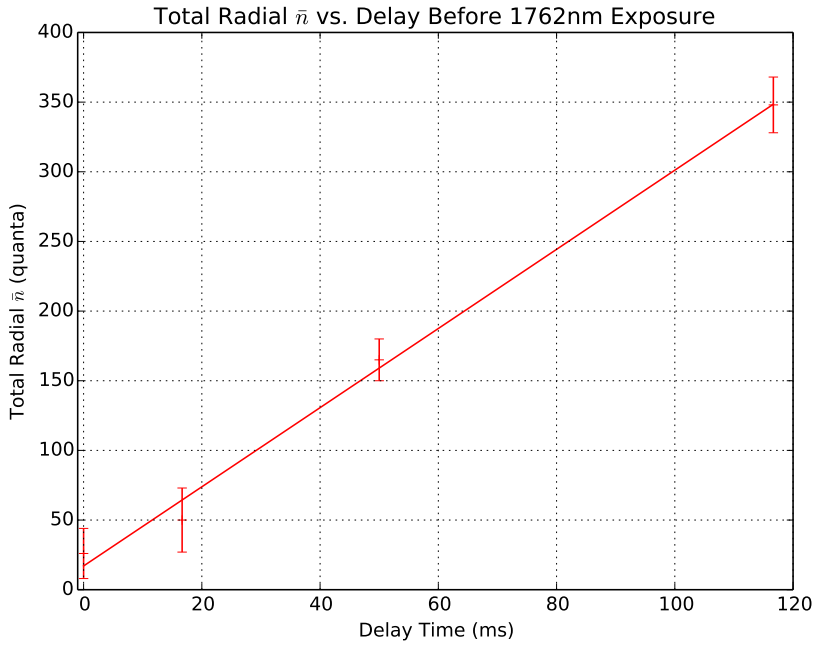

Figure 6.4: Measured radial motional average occupation numbers as a function of the period of time the ion was allowed to heat before the 1762 nm pulse began.

where σ_f is the width of the approximately gaussian spread of frequencies ($\approx$ 20 kHz), μ_f is the center of this distribution which is approximately equal to $\omega_{\text{transition}}$ which is the center of the 1762 nm transition, Ω_{rabi} is the rabi frequency ($\approx$ 50 kHz with our achievable laser power). The resulting curve also exhibits a loss of contrast on the 100 us time scale.

Given the approximate width of this noise we can combine the two preceding equations and fit our Rabi flops to this curve. The fit parameters are the Rabi frequency Ω, the optical pumping efficiency s, and the sum of the radial average thermal occupation numbers $\sum_i \bar{n}_i$. In Figure **??**, the heating rate of the radial modes is again approximately linear, with an initial temperature that is reasonable for a Doppler cooled barium ion. The linear fit shown corresponds to an initial $\sum_i \bar{n}_i = 17$ quanta, with a heating rate of 2.84 quanta/ms.

The heating rate after the correction for the 1762 nm laser noise is similar to the uncorrected heating rate, and it seems that the two losses of contrast have approximately

the same effect. There does not seem to be any new behaviour when the two sources act together. We will use this measure of our single ion heating rate to consider our results with ion chains in the next section. We expect that the heating rate per ion should be approximately constant for small numbers of ions because their trapping environment is very similar.

6.2 Mixed Species Ion Chains

In order to analyze transferring quantum information between ions we first need to understand the normal mode structure of a chain of ions. Since we are working with multiple ion species we will also consider the case that the mass of each ion may be different. The normal modes for any given number of each species of ion and any ordering of those species can easily be calculated through normal classical mechanical techniques. When the dynamics are much slower than the rf period the Mathieu equation can be ignored and the trapping potential can be written as a simple harmonic oscillator. The base trapping potential is then

$$V_{\text{trap}} = \omega_x x^2 + \omega_y y^2 + \omega_z z^2, \tag{6.10}$$

where ω_z is the axial confinement generated by the dc electrodes that is necessarily weaker than ω_x and ω_y. The radial secular frequencies are a function of the ion mass and therefore are different for the different ion species. This interaction is modified by the Coulomb interaction between the ions

$$V_{\text{coulomb}} = \sum_{i=1}^{N} \sum_{j \neq i} \frac{1}{4\pi\epsilon_0} \frac{e^2}{|\vec{x}_i - \vec{x}_j|}, \tag{6.11}$$

where N is the number of ions in the trap and e is the proton charge (we have assumed the ions are singly ionized).

Near the bottom of the potential well, the linear terms are zero and the potential can be approximated by

$$V_{ij} = \frac{1}{\sqrt{m_i m_j}} \frac{\partial}{\partial x_i} \frac{\partial}{\partial x_j} (V_{\text{trap}} + V_{\text{coulomb}}) \tag{6.12}$$

neglecting the constant potential. The equations of motion are then given by

$$\ddot{x}_i + V_{ij} x_j = 0. \tag{6.13}$$

There are 3N solutions which take the form of independent harmonic oscillators. Each harmonic oscillator corresponds to motion along one of the eigenvectors of the matrix V_{ij} with an angular frequency ω equal to the square root of the corresponding eigenvalue. The analysis of sideband transitions still carries through with one small modification. The separate motional state operators for each ion and each mode now carry the corresponding eigenvector component as a scalar multiple that reduces the motion of the ions over the single ion case. This effect can be accounted for by defining our Lamb-Dicke parameter for each mode α and ion i to be $\eta_{\alpha,i} = e_{\alpha,i} x_{\alpha,0} k_x$.

Scanning these radial modes can follow almost the exact procedure described for scanning over the radial modes with a single barium ion. One difference is that state detection must be done with our EMCCD camera instead of with the PMT. The PMT has no spatial sensitivity and cannot distinguish which ions in the chain are shelved. I have developed software that integrates our experiment with the EMCCD camera and automatically detects shelving events for all ions in a chain.

One additional difference is that data can only be collected when the ions are ordered in one particular configuration. Performing experiments involving these mixed species chains is complicated by the fact that the normal mode structure changes depending on the ordering of the ion species in addition to the numbers of each ion. In the future, this work can be done in microfabricated traps where dc control voltages can be used to separate, reorder, and merge ions. At the moment the ions are randomly reordered by shuttering the Doppler cooling beams and allowing the ions to heat for a period of time. When the ions recrystallize their order may have randomly changed to the correct order. Since this procedure is entirely random it becomes more unlikely to reach the correct configuration as the number of possible configurations increases.

We have performed initial characterizations of chains of two barium and two ytterbium ions. This chain length is short enough that we can achieve the correct ion ordering enough of the time to take reasonable amounts of data. It is long enough to allow us to investigate the effects of clustering or distributing the barium ions throughout the chain. We are most interested in how effectively the ytterbium ions can be kept cooled by Doppler cooling the barium ions.

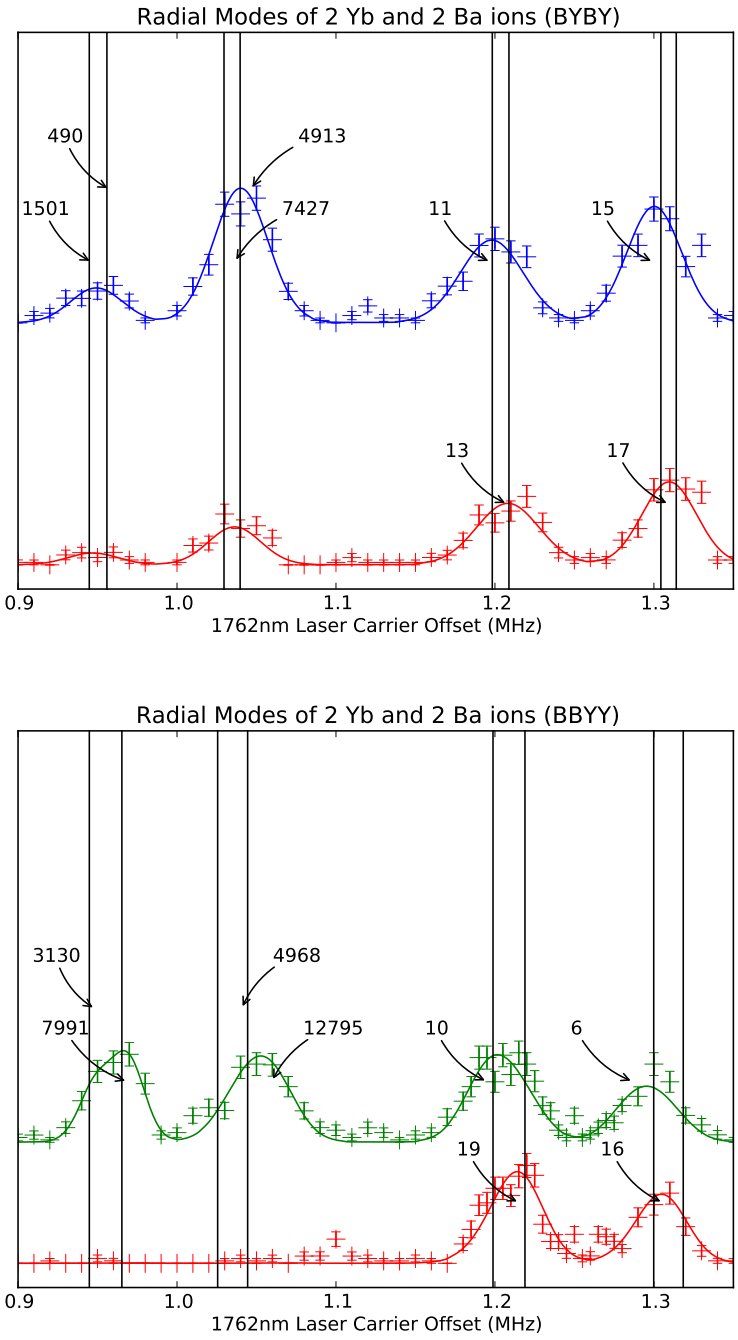

Figure 6.5: Shelving probability as a function of frequency detuning of the 1762 nm source. Multiple radial sideband transitions can be seen and their strengths are fit to average thermal occupation numbers.

First we will consider the case where the barium ions are maximally dispersed in the ion chain. In order the chain is composed of barium, ytterbium, barium, and ytterbium. In Figure **??**, a sample radial mode scan in shown. The two data curves are the probability of shelving the barium ion in that position as a function of the 1762 nm laser detuning. The second curve is offset from the first to be more easily visible. In both cases the shelving percentage does not exceed 35% and has been kept deliberately low to allow us to fit each peak to the weak excitation limit. In this limit, the shelving probability is given by

$$P_{\text{shelve}}(\omega) = \frac{1}{4}\eta_{\alpha,i}^2 \bar{n} \Omega_i^2 t^2 \frac{\sin^2((\omega - \omega_\alpha)t/2)}{(\omega - \omega_\alpha)^2/4}, \tag{6.14}$$

where Ω_i is the Rabi frequency of the 1762 nm laser on ion i, ω_α is the angular frequency of normal mode α. In order to find Ω_i we also perform a Rabi experiment as described above and measure the Rabi frequency for each ion by fitting to the resulting curve. Again we have to deal with the awful 1762 nm lock by allowing the 1762 nm frequency to vary over some range of frequencies. Therefore, we actually fit the radial sideband curves to the integral of Equation **??** over a Gaussian band of frequencies around the center frequency of the 1762 nm laser. This fitting as the effect of broadening all of the radial modes far beyond their natural linewidth and making it more difficult to fit the heights of modes close together in frequency.

The radial mode frequencies and eigenvectors are found by the numerical procedure above, but the measured radial mode frequencies display small 10 kHz to 20 kHz shifts from these frequencies. We believe these shifts are due to small offsets in the error signal of the 1762 nm laser. The ZeroDer cavity that it is locked to also displays mechanical relaxation at a rate of 10 kHz/day, which explains some of the shifts because of the 6 hour experimental run time. For this reason we must also allow the angular frequency of each mode to be changed by some small amount in order to fit the data.

Figure **??** shows the predicted radial modes given our independently measured trap secular frequncies as black vertical lines. The positions of the modes after the small frequency shifts are fit to them are indicated by the positions pointed to by the arrows, which label the fit $\bar{n}$ to each peak. The four lowest frequency modes have large eigenvector motional components in ytterbium ions, but very small motional components for both barium ions. It is

Ba, Yb, Ba, Yb Radial Mode Data

Frequency (MHz)	Barium Eigenvector Components		$\bar{n}$
1.30	0.989	0.143	17
1.29	-0.144	0.989	15
1.20	0.988	0.148	13
1.19	-0.150	0.987	11
1.03	0.003	0.034	4913
1.02	0.028	0.034	7427
0.95	0.003	0.039	490
0.94	0.033	0.041	1501

Table 6.1: Eigenvector components and occupation numbers for each mode in a chain of Ba-Yb-Ba-Yb ions. The modes coupled strongly to ytterbium have much higher occupation numbers.

clear that these modes are not being well cooled by the barium ions. The mode frequencies, barium eigenvector components, and $\bar{n}$ for this configuration are given in Table **??**. It is clear that there is a very large difference in the amount of motion that the last four modes have in barium ions than the first four. We can also observe that having both eigenvector components be of the same magntiude does not decrease the number of quanta in the mode signifcantly, but even slightly increasing the maximum eigenvector component can have large effect. Additionally, the participation of the barium ions is increased when the base secular frequency for that direction is smaller.

When we move all of the barium ions to one side of the chain such that the order is barium, barium, ytterbium, then ytterbium we measure the occupation numbers from Table **??**. The temperature of the decoupled modes has increased substantially. It is very clear from the eigenvector components of these modes and from Figure **??** that the outermost barium ion is even more stongly decoupled. It is fairly easy to conclude that for any reasonable chance of cooling all of these modes using barium ions, the barium ions will have to be interspersed along the length of the chain.

Ba, Ba, Yb, Yb Radial Mode Data

Frequency (MHz)	Barium Eigenvector Components		$\bar{n}$
1.31	0.866	0.500	16
1.29	-0.500	0.865	6
1.20	0.865	0.501	19
1.18	-0.501	0.864	10
1.03	0.002	0.022	12795
1.01	0.002	0.029	4968
0.95	0.002	0.026	7991
0.93	0.002	0.035	3130

Table 6.2: Eigenvector components and occupation numbers for each mode in a chain of Ba-Ba-Yb-Yb ions. The modes coupled strongly to ytterbium have much higher occupation numbers.

In order to gain a simplifed understanding of what this data tells us about the temperature of ions in mixed species ion chains, we tried comparing the $\bar{n}$ for each radial mode that is not cooled well by barium to its eigenvector components for barium ions. The correlation between these variable seems to be strongest when we compare the $\bar{n}$ to $max\,|e_\alpha|^2$. Plotting these against each other shows a strong correlation, with reasonable thermal occupation numbers only being reached when the eigenvector component $e_\alpha \approx 0.04$.

Obviously cooling ytterbium ions using only barium cooling lasers is not going to be as efficient as we would hope. It seems that that our Doppler cooling is still near optimal for barium ions, so it is unlikely that Doppler cooling alone will be able to perform any better than this. There are still a few options for making progress however. For the weaker of the two trap axes, we can see that the ytterbium modes are reasonably cold for chain configurations that are well mixed. Only a few modes of the trap will need to be kept cold to perform entangling gates in ytterbium, and its possible the trap strengths and ion configuration can be arranged to make this possible. Doing so will likely require the barium to be well distributed thoughout the chain.

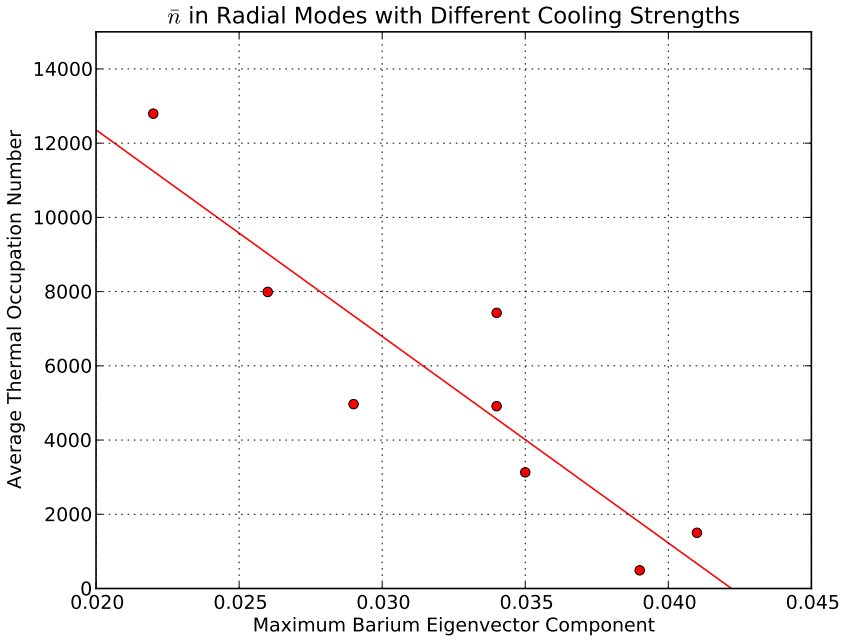

Figure 6.6: Radial $\bar{n}$ as a function of the maximum eigenvector component with a barium ion squared. The linear trend is given as a guide to the eye.

Investigating these problems for increasing numbers of ions should prove very itneresting. If the trends established above continue to hold it may still be possible to keep a few modes cold enough to be in the Lamb-Dicke regime and perform entangling operations in ytterbium. Working with more ions will most likely involve moving this experiment to a surface electrode trap where the ordering of the ions can be easily controlled. Scaling this experiment further in its current trap would be very difficult.

6.3 Ion Species Reordering

Working with mixed ion species chains gives an experimenter the ability to determine when chains reorder. Obviously when working with only a single ion species, the ions are indistinguishable and it is impossible to tell whether its order is the same as previously at any point in time. We hypothesized that the reordering of ions would happen at a relatively constant temperature and therefore could provide a simple temperature or heating rate measurement. To investigate this hypothesis we performed simulations of the motion of mixed ion species chains.

Heating in ion chains is difficult to simulate well because it often depends on random electric field noise which is difficult to integrate numerically. Instead of simulating the heating process, the ions are initialized at the beginning of the simulation to a given temperature. Depending on this initial temperature, we track the probability for them to reorder before they are cooled to somewhere near their ground state. The initial temperature is modeled by initializing the ions velocity to the corresponding energy with a random direction. The ions motion is then modeled subject to the differential equation

$$m\ddot{\vec{x}} = F_{\text{trap}} + \hbar\vec{k}\frac{\Gamma}{2}\frac{s}{1+s+4\left(\frac{\delta+\vec{k}\cdot\vec{v}}{\Gamma}\right)^2} + \sum_{i\neq j}\frac{1}{4\pi\epsilon_0}\frac{e^2}{|\vec{x}_i-\vec{x}_j|^3}\left(\vec{x}_i-\vec{x}_j\right), \tag{6.15}$$

where $\vec{x}_i$ is the position of the ion that begain in position i, F_{trap} is the harmonic trapping forces that confine the ions, $\vec{k}$ is the wavevector of the cooling lasers. The integration is performed using the Boost odeint numerical integration library. At the end of this procedure, it is determined whether the ion species have reordered in a way that is experimentally detectable, which is to say that the species are in a different configuration. Figure **??** shows

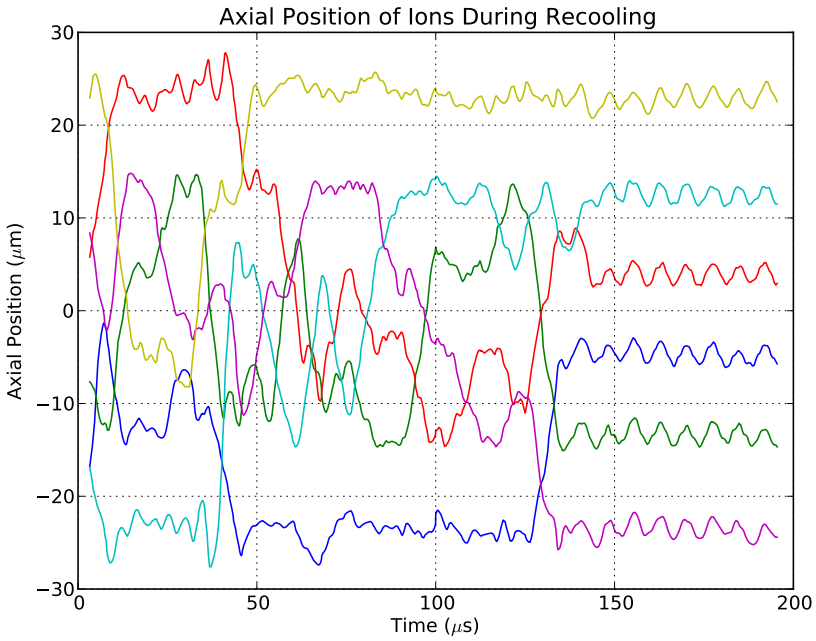

Figure 6.7: Simulated axial positions of ions as function of time. The ions begin with a large randomly directed velocity and are slowly cooled by simulated Doppler cooling.

a subset of the axial positions of a chain of ions from a single run of the simulation where the ions reorder. Repeating this process several thousand times for several temperatures shows us that the probability to reorder changes relatively sharply with temperature. Using a single quad-core desktop the runtime for performing 10,000 iterations of this procedure is almost a day because of the difficulty of integrating singular potentials and the long integration times used to be sure that all of the dynamics of the ino trap have been modeled.

Experimentally, this phenomenon is very easy to observe. Once again heating can be caused by allowing the ion to spend several milliseconds uncooled in the trap. Using our EMCCD camera we image the ions before and after a given time period of uncooled time. The reordering probability is then extracted from a series of many such experiments. In order to fit the collected data to the theory curve generated before need to fit the initial temperature and heating rate of the ion chain.

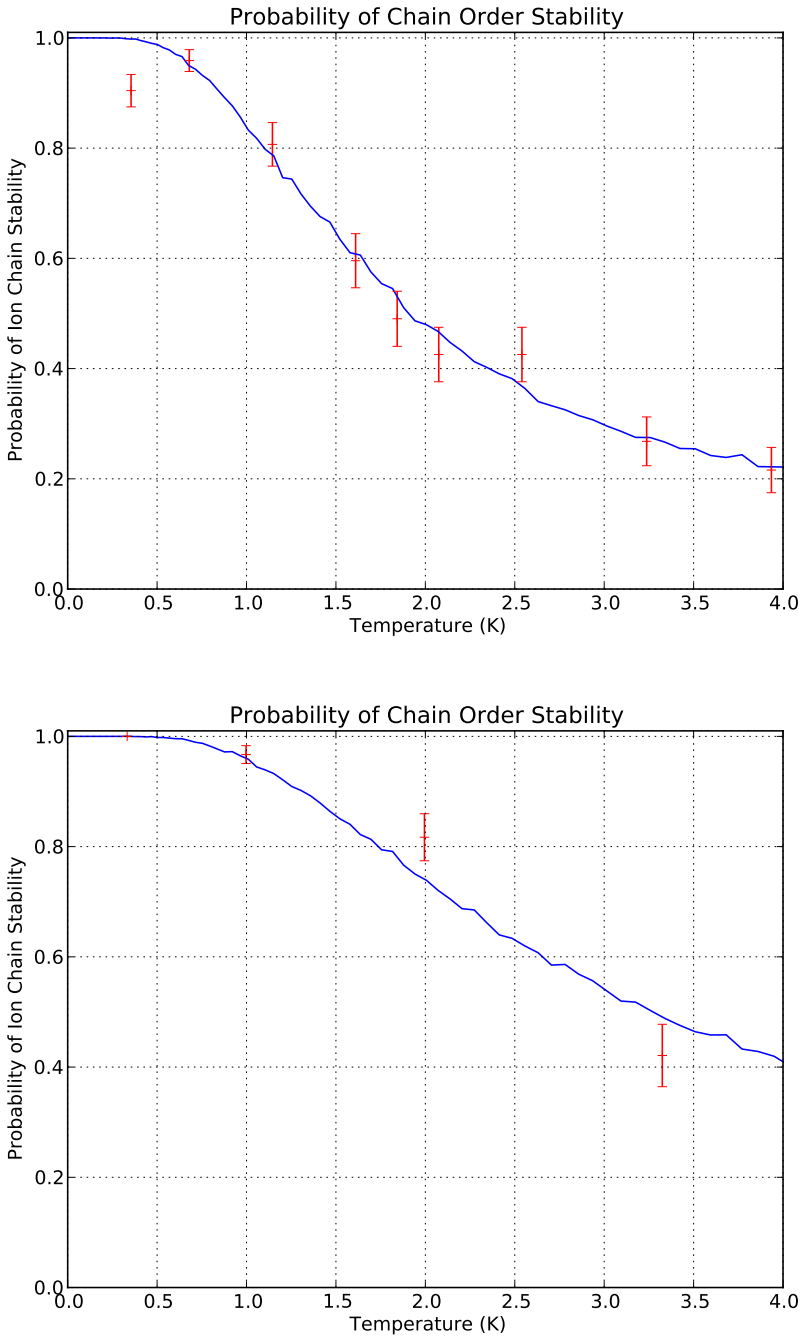

Figure 6.8: Reordering probability as a function of temperature. The simulation results are shown in blue, while the red data points are taked at different uncooled times and then fit to temperatures using a linear heating rate. For seven barium and one ytterbium ion (top) the initial temperature is 0.215 degrees Kelvin and the heating rate is 0.465 K/s. For five barium and one ytterbium (bottom) the initial temperature is 0 K and the heating rate is 0.665 K/s.

In Figure **??**, the resulting curves for an ion chain of 7 barium and one ytterbium ion are shown fit to one another. The initial temperature is 0.215 degrees Kelvin and the heating rate is 0.465 K/s. For five barium ions and one ytterbium ion the initial temperature is 0 K and the heating rate is 0.665 K/s. Obviously, this initial temperature is not physically realistic and is probably caused by the small amount of data taken using the smaller chain. More data would have had to be taken to fit a reasonable initial temperature because its effect on the fit is relatively small. The heating rate measurement should be reliable because it has a strong effect on the generated points.

The advantage of this technique is that a single, fast measurement can quickly characterize the heating rate of the trap. With the methods described earlier in this chapter several dozen data points each comprised of several hundred experimental runs must be performed to fit a function and determine the ions' temperature or heating rate. With this method, collecting one or two data points near the maximum slope of the reordering probability can generate a quick measurement of the same quantity. The reordering measurement also does not require any narrow transitions to be addressed, so traps can quickly be characterized even before these additional lasers are aligned to them.

Since these measurements are so quick to carry out, it is also convenient to look at how our Doppler temperature varies with our 493 nm laser frequency using this technique. Figure **??** plots the reordering probability as a function of the detuning of this main barium cooling laser with the uncooled time in the experiment set to the maximal reordering slope. Collecting this data using this method took only a few minutes as compared to an hour or more to measure several curves with the other methods described. For this reason, reordering measurements also serve as a good, fast indicator of cooling efficacy. Although we saw earlier that this technique is not always a good measurement of initial temperature, when sitting on this maximal slope we can definitely see the effects of the Doppler cooling parameters.

In this chapter we have characterized the temperature and heating rate of barium and ytterbium ions in our trap in many different ways. The benefit we were hoping to achieve in designing this system was the ability to continuously cool barium ions while performing quantum operations with ytterbium ions. It certainly looks like that task is not going to be

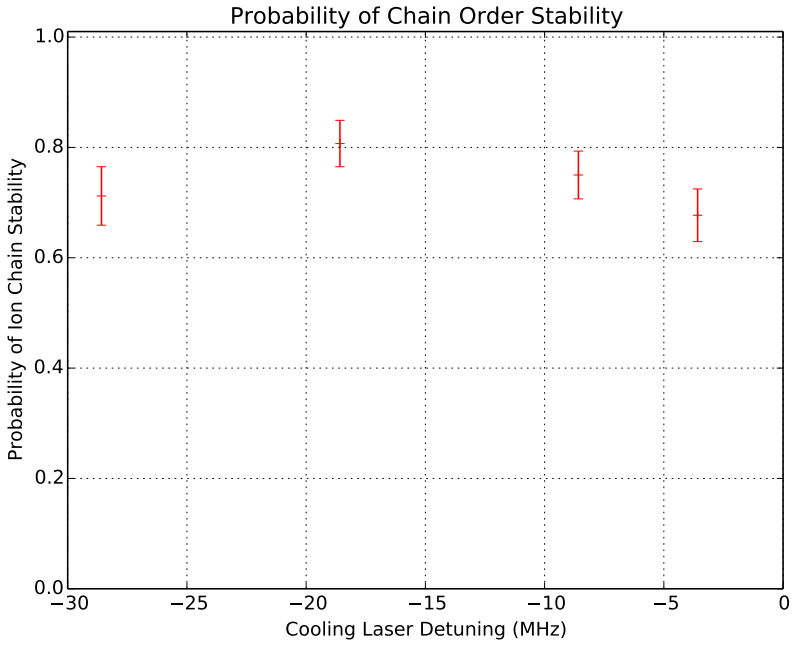

Figure 6.9: Reordering probability after 2 seconds of uncooled time as a function of the frequency detuning of the barium cooling laser.

as easy as we had hoped. In Chapter **??**, we found that we needed to be operating in the Lamb-Dicke regime where $\bar{n}\eta \ll 1$ in order for our ion entangling operations to have high fidelity.

Chapter 7

QUANTUM OPERATIONS

As we make progress towards effectively cooling these ion chains we want to begin exploring how effective quantum operations can be engineered in ions in them. We have begun performing single qubit quantum gates with barium ions in our system, and are preparing the necessary equipment to being characterizing entangling gates. Although these single qubit rotations are simplistic we will soon be able to start using them to explore quantum coherence in this system.

7.1 Zeeman Transitions

The Zeeman qubit I have described in barium as well as the hyperfine qubit in ytterbium have large magnetic moments. Coherent control of these qubits can be implemented using oscillating magnetic fields. In our group we have some traps that have been designed to accomodate applying large magnetic fields to ions by placing good conductors along paths inside of the vacuum chamber near the ion. Our quantum information vacuum chambers were not designed to incorporate this feature, and for the moment we are applying the fields from outside them.

We have demonstrated our ability to find and drive Zeeman transitions using an external field coil driven by a Stanford SRS-345 frequency source. The field coil is composed of approximately 20 turns of copper wire and is located on our imaging viewport as close to the ion as possible. The rf can be crudely coupled onto this coil by making a basic resonant circuit by adding capacitance to cancel the coil's inductance near the Zeeman transition frequency.

The experimental procedure to observe these transitions again begins by switching the cooling lasers to perform optical pumping and pumping the ion into one of the Zeeman states, which I will call $|0\rangle$. The cooling lasers are then shuttered and we attempt to drive a

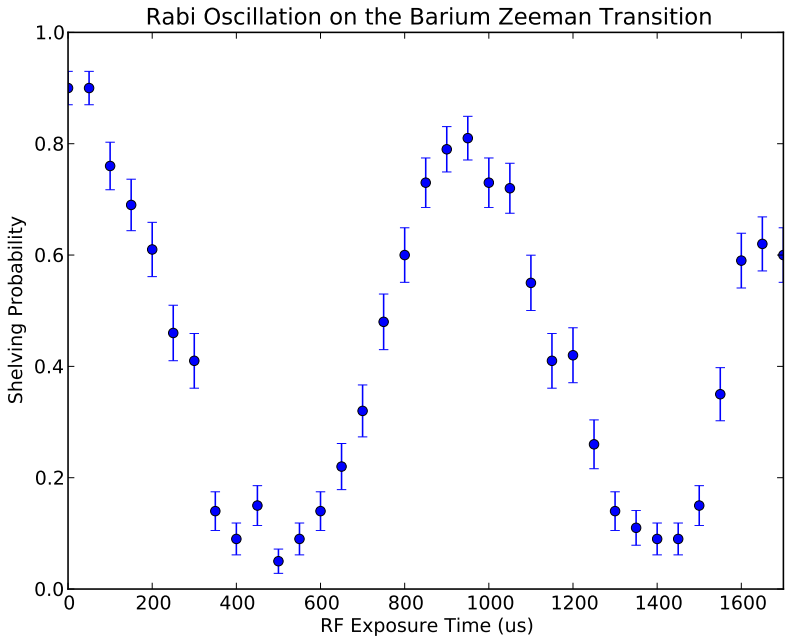

Figure 7.1: Rabi oscillations between the barium ground state Zeeman levels are shown as a function of the interaction time with the resonant rf source.

Zeeman transition at our Zeeman transition frequency $\omega = 14.610$ MHz. After this attempt we apply a π-pulse of 1762 nm light the drive $|0\rangle$ to some Zeeman level in the $5D_{5/2}$ state of barium with a probability of approximately 90%. Finally, we reactivate the cooling lasers and the ion flouresces if it has not been successfully shelved into the $5D_{5/2}$ state.

For our initial characterization of this process, we have only been able to apply relatively small magnetic fields to the ion. Figure **??** shows the shelving probabilty as a function of the exposure time of our rf source tuned to resonate with the Zeeman transition. The beginning of a Rabi oscillation is clear, but then the frequency and amplitude of the transition begin to change. These changes are due to the changing magnetic field in the trap because of the ac wall phase. All of our magnetically sensitive experiments are triggered to begin on a maximum of the ac wall voltage, but since this experiment lasts for several milliseconds we begin to see the magnetic field shift.

The fidelity of this qubit operation is currently low, but it demonstrates that we have the infrastructure to support these kinds of operations. The fidelity could be quickly improved by using amplifiers and resonators to apply a stronger magnetic field to the ion. Increasing our magnetic field would allow us to minimize the size of the magnetic field drift. Our maximum shelving probability could also be signifcantly improved by carefully improving our optical pumping efficiency and Doppler cooling efficiency. In actual quantum information processing it will be more important to improve the fidelity of the qubit rotation operations because many of these operations must be performed before a single measurement in a quantum operation. The accumulation of errors in qubit operations over the course of algorithms is going to be one of the next challenging problems to address in trapped ion quantum computing.

7.2 Raman Transitions

The difficulty with performing qubit rotations using this direct technique is that the energy separation between ideal qubit levels can often be very small. Therefore, near resonant radiation will have a long wavelength and be difficult to address onto single ions. For example, the qubit we will address in $^{171}Yb^{+}$ has an energy splitting of approximatel 12 GHz, which corresponds to radiation with a wavelength of approximately 2.5 cm. Typical ion separations in a single trapping region are 5 um to 10 um. For performing quantum algorithms where we need to perform different rotations on adjacent qubits we will need to implement additional controls.

One possible strategy for individually addressing these qubit levels is the shift the qubit energy spacing using a magnetic field gradient or ac Zeeman effect. If these frequency shifts can be localized onto one ion, fields resonant with individual ions can be applied provided the transition is driven slowly enough. With a carefully designed control system and control of the applied pulse, the fidelity of these operations can be very high.

The strategy we will be utilizing is to use optical Raman transitions. Using Raman transitions is advantageous because the optical beams driving them can easily be focused onto individual ions, and the photons absorbed and emitted carry much more momentum and therefore couple strongly to the motion of the ions. The interaction between optical

transitions and the motional modes of the trap is still characterized by the Lamb-Dicke parameter $\eta = k_{\text{photon}} x_{\text{ion}}$. In order to generate entanglement between ions we need to drive two transitions that change the state of one of the traps modes of motion, so increasing our Lamb-Dicke parameter is beneficial.

The initial infrastructure for performing Raman transitions is all avilable at this point in time. We will be using a mode-locked diode-pumped ND:YVO_4 laser to provide the optical beams. This laser was originally a pump laser for our Ti:Sapphire mode-locked laser, but it has been modified to support mode-locked operation itself. Mode-locked operation is favored by a semiconductor saturable absorber end mirror that has been added to the laser cavity. In addition, the cavity had been modified to produce the necessary tight focus on the saturable absorber [**?**, **?**]. The laser produces 2 W of optical power at 1064 nm that we then frequency double using a single pass LBO crystal to 500 mW of 532 nm light. The output pulses were measured using an autocorrelator to have 17 ps pulse times and repition rates are approximately 150 MHz.

The electric field from a mode-locked laser can be described by

$$\vec{E}(t) = \vec{E}_0 \sum_{n=0}^{\infty} f(t - nT) \cos(\omega t + kx) \tag{7.1}$$

where the function f describes the pulse shape of the laser and T is the time period between pulses. In an optimal mode-locked laser $f(t) \propto \text{sech}(\pi t/\tau)$, where τ is the time duration of the pulses. Taking the Fourier transform of this field we can find that it has many sharp spectral components separated by the repetition rate of the laser in a range of frequencies around ω. These "comb teeth" can be used to drive narrow atomic transitions.

We will be using these comb teeth to drive Raman transitions between our qubit levels. Therefore we require that the bandwidth of the laser is sufficiently larger than our qubit energy spacing that many of the comb teeth can contribute to driving transitions. The electric field magnitude of each comb tooth E_n can be found from the envelope function f and the center frequency of the bandwidth of the laser. The resulting Raman transition will have a coupling strength given by

$$\Omega = \frac{\mu^2 E_n E_{n-q}}{\hbar \Delta} \tag{7.2}$$

By driving Raman transitions with detunings of $\omega_{\text{qubit}} \pm (\omega_{\text{motional}} + \delta)$, we can use these lasers to generate entanglement between ions using the Mølmer-Sørensen gate. For our 532 nm light driving Raman transitions in barium, we must consider coupling through both the $6P_{3/2}$ and the $6P_{1/2}$ state. I estimate that given our current laser power we can expect to drive carrier Raman transitions at a rate of $\Omega \approx 100$ kHz. The Mølmer-Sørensen coherent two qubit operation can be driven at a rate of $2\eta\Omega \approx 10$ kHz. These rates should be sufficient to demonstrate a universal set of gates in barium.

In order to drive Raman transitions using this system we need to split the pulse train into two beams and frequency detune these beams from each other. We have accomplished this using two AOMs. A base 220 MHz signal is generated by an HP-8640B signal generator and then split into two paths by a rf power splitter. One path continues directly to a high speed rf switch, while the other is mixed with a computer controlled Stanford Research Systems DS345 20 MHz signal generator and then sent to a different switch. Both paths are then amplified by 200 MHz rf amplifers and sent to separate 200 MHz AOMs which together severely attenuate the 240 MHz mixed signal leaving the AOMs to be driven by the 200 MHz and 220 MHz signals. The common mode 200 MHz signal has no effect on Raman transitions and so the stability only depends on the DS345 signal and there is no need to phase lock two rf sources together. This optical setup is operational with both beams controlled by the AOMs and focused onto the trap. The path length between the two beams is set by a linear delay stage, and the path difference has been measured to approximately overlap the two pulses temporally as well. Since we know the separation of the Zeeman levels because we have directly driven them, there are no remaining degrees of freedom in the system.

In the future we plan to provide the rf for the two Raman beams with a two channel DDS based on the Analog Devices AD9958 part. The two channels are controlled through a serial interface and are phase coherent because they are created from the same reference clock. This device will also allow us to provide feedback to stabilize the frequencies of the comb teeth against path length drift in the optical cavity. We will also be able to program pulse sequences with different amplitudes and phases into the DDS to perform error-compensating pulse sequences.

These techniques have been developed using commercial systems by several other ion trapping groups. Mølmer-Sørensen gates with 10 to 100 μs π time have been developed [**?**]. The bandwidth of the modelocked laser is also sufficient to span the 12.6 GHz hyperfine splitting in ytterbium ions to drive entangling gates beteween these levels. As we develop our ability to work with quantum information in ytterbium, this laser will become increasingly important. In order to work with ytterbium, we can use a second double crystal to generate the third harmonic of the laser frequency at 355 nm, which is at an optimal frequency detuning for ytterbium [**?**].

7.3 Conclusions and Outlook

The initial infrastructure for working with mixed species ion chains in a quantum computer architecture has been described here and implemented in my lab. I have developed the technology that we will use to work with surface electrode ion traps in the future. These traps will be able to stably confine more ions in each trap and hold multiple separate trapping regions within the same vacuum chamber. The additional voltage degrees of freedom will also allow us to control the trapping potential the ions experience within each trap. We have demonstrated using this ability to shuttle ions around the surface trap and perform experiments in different locations to explore the local features of these traps. Initial measurements of stray fields and heating rates have been made that will guide us in improving our cooling and trapping apparatus in the future.

We can repeatably trap barium and ytterbium ions and stably confine and cool them. Currently the temperature of some of the modes of the ytterbium ions will be problematic for implementing entangling gates, but there are many possible avenues for overcoming this problem. One of the main difficulties in performing these experiments at the moment, is that in the macroscopic Paul trap we are working in the ordering of the ions is random. When we perform experiments involving the motional modes of the ions we need a particular configuration of the two species, and the only method we have to achieve this is repeatedly heating the ions until the ion crystal melts and then recrystallizing it. As we move the techniques we have developed into surface electrode traps we should be able to perform experiments with tens of ions with full control over the number and configuration of the

cooling ions.

Lastly, although most of my work has gone into the basic trapping and cooling infrastructure for our scalable system, we have made some progress towards performing actual quantum gates using this system. We have found and driven our Zeeman qubit level in $^{138}Ba^{+}$, which will enable us to rapidly set up our actual quantum operations procedures with the Vanadate laser. All of the set up on that laser is complete and we are beginnin experiments to attempt to drive carrier transitions. This system will allow us to begin testing how well all of the infrastructure we've developed will work during actual quantum computation. That is an exciting step.

Overall the future for trapped ion quantum computing still looks promising. All of the required basic systems have been implemented, and the only remaining challenge is having a sufficient number of communicating ions. As you most certainly know by now, there are a huge number of different ways we can approach this goal. We have been simultaneously working in several directions on this problem, and as we begin to combine these ideas into larger systems I think we'll be able to achieve some really amazing things.

VITA

John Albert Wright was born on May 9^{th}, 1988 to Juli and William Wright in Chapel Hill, North Carolina. He eventually moved to Indianapolis and graduated from North Central High School in 2006. Continuing his education, he received a Bachelor of Science degree majoring in Physics, Math, and Computer Science from Purdue University in West Lafayette, Indiana in 2010. He joined Boris Blinov's ion trapping group at the University of Washington in July, 2010, and had the opportunity to develop a completely new lab devoted to quantum information research. He graduated with a Physics Ph.D. from the University of Washington in March 2015, and hopefully moved on to fulfilling career.